# Title:

# Cell-type specific optogenetic fMRI on basal forebrain reveals functional network basis of behavioral preference

Yijuan Zou[1,4], Chuanjun Tong[1,4,*], Wanling Peng[1], Jiangxue Li[1,2], Ying Xia[1], Mengchao Pei[1], Kaiwei Zhang[1], Weishuai Li[1], Min Xu[1,3,*], Zhifeng Liang[1,3,*]

[1] Institute of Neuroscience, CAS Key Laboratory of Primate Neurobiology, Center for Excellence in Brain Science and Intelligence Technology, Chinese Academy of Sciences, Shanghai, China

[2] University of Chinese Academy of Sciences, Beijing, China

[3] Shanghai Center for Brain Science and Brain-Inspired Intelligence Technology, Shanghai, China.

[4] These authors contributed equally

*Correspondence should be addressed to Chuanjun Tong (tongcj@ion.ac.cn) or Zhifeng Liang (zliang@ion.ac.cn) or Min Xu (mxu@ion.ac.cn).

# Graphic abstract:

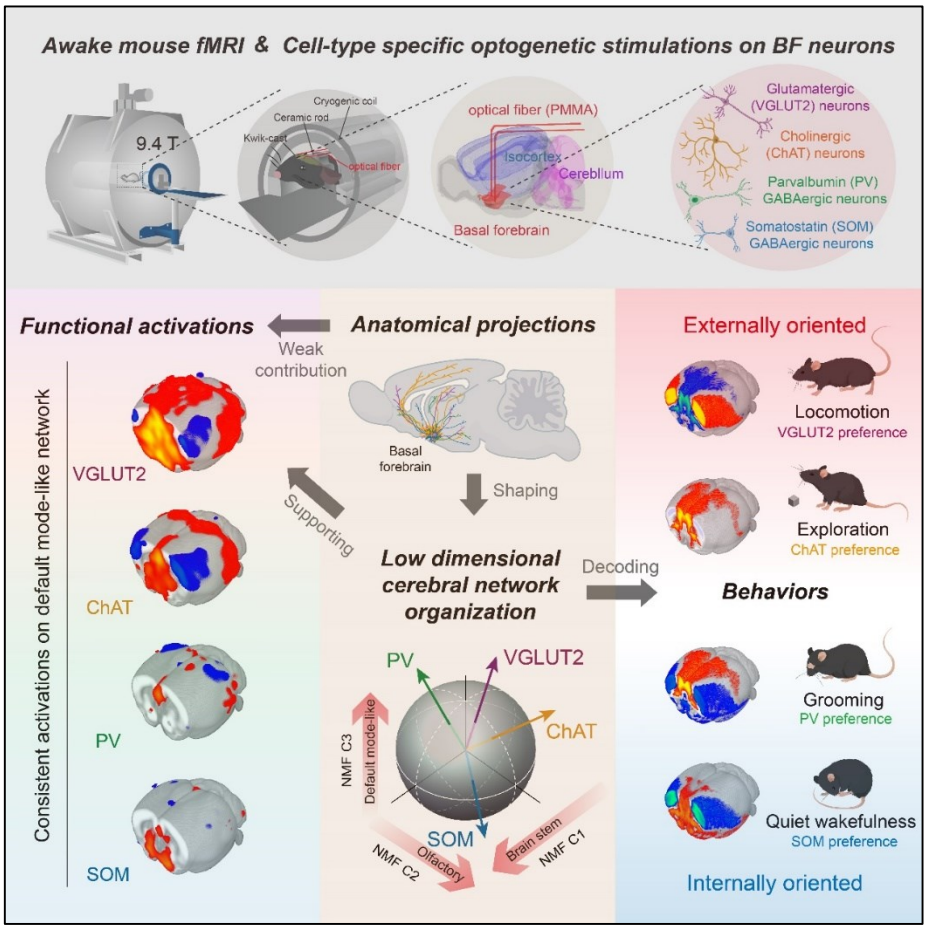


## Highlights:

- Optogenetic stimulations of basal forebrain (BF) neurons evoked distinct cell-type specific whole-brain BOLD activations.
- Optogenetic activation of inhibitory (PV and SOM) or excitatory (VGLUT2 and ChAT) neurons in BF drove internally or externally oriented behavior respectively.
- A decoding model linking the BF-modulated BOLD activations, low dimensional structural networks, and behavioral preference revealed a functional network basis of BF-modulated behavioral preference .

# Abstract

The basal forebrain (BF) is an anatomically and neurochemically complex structure that plays key roles in regulating various brain functions. Although BF is best known for cholinergic neurons that influence functional network dynamics and behaviors, non-cholinergic neurons are the dominant neuronal population in BF, and are found to contribute as well. However, it remains unclear how cholinergic and non-cholinergic BF neurons modulate large-scale functional networks and their relevance in intrinsic and extrinsic behaviors. With our optimized awake mouse optogenetic fMRI approach, we revealed optogenetic stimulations of four BF neuron types evoked distinct cell-type specific whole-brain BOLD activations, which could attribute to BF-originated low dimensional structural networks. Optogenetic activation of inhibitory (PV and SOM) or excitatory (VGLUT2 and ChAT) neurons in BF drove internally or externally oriented behavioral preference, respectively. Furthermore, we uncovered the functional network basis of the above BF-modulated behavioral preference, through a decoding model linking the BF-modulated BOLD activations, low dimensional structural networks, and behavioral preference. To summarize, we decoded a functional network basis of differential behavioral preference with cell-type specific optogenetic fMRI on BF, and provided an avenue for investigating mouse behaviors from a whole-brain view.

# Introduction

The basal forebrain (BF) is a set of heterogeneous telencephalic structures on the medial and ventral parts of the cerebral hemispheres[1,2]. The basal forebrain is most commonly known as a key cholinergic brain region[1–3]. However, cholinergic neurons only represent 10–20% of all BF neurons, and much more non-cholinergic neurons, including glutamatergic, parvalbumin-positive (PV) and somatostatin-positive (SOM) GABAergic neurons, are present in BF[1–3]. Previous studies reported that the above four types of BF neurons exhibit both complex local connectivity and long-range projections to the cortex[3,4]. Traditionally, studies of BF have focused on its cholinergic neurons and revealed its involvement in a variety of brain functions, including arousal, attention, memory, learning, motivation and reward both in health and diseases[5–12]. However, BF non-cholinergic neurons were also found to contribute to many brain functions as well[3,13–17].

As the cholinergic and non-cholinergic BF neurons all have large-scale cortical and subcortical projections, it is long speculated BF may contribute to the whole-brain functional network dynamics. One recent human fMRI study found global BOLD signal peaks coincided with negative activations in BF, which was associated with arousal fluctuations[18]. Another macaque fMRI study showed unilateral inactivation of BF with muscimol resulted in a decrease in the amplitude of BOLD signal in ipsilateral regions, which receive strong projection from BF neurons[19]. Both studies suggested that the extensive variations in large-scale cortical activity observed through fMRI were linked to BF, which was assumed to be contributed by BF cholinergic neurons. However, in those two studies, direct evidence was lacking to attribute such modulation to BF cholinergic system.

Specific modulation of the cholinergic system, combined with rodent fMRI, revealed its impact on large-scale network activity[20–22]. Chemogenetic activation of BF cholinergic neurons[22] or pharmacological inhibition of the cholinergic system[20,21] in anesthetized rats, both demonstrated significant decreases in functional connectivity (FC) and BOLD amplitude within the default mode-like (DMN-like) network, which appears contradictory. Neurophysiological studies in rats showed gamma oscillations were synchronized and of

high gamme power between the BF and DMN-like nodes (i.e., anterior cingulate area (ACA), retrosplenial cortex (RSP)) during internally oriented behaviors, such as quiet wakefulness and grooming[23,24]. Furthermore, optogenetic activation of BF PV neurons enhanced BF gamma oscillations and promoted grooming behavior[25], suggesting the regulation of non-cholinergic neurons to DMN-like network and internally oriented behavior. However, It remains unclear the relationship among the cell-type specific BF modulations, large-scale functional networks and their behavioral relevance.

Therefore, in this study, we established a decoding model to link the BF-modulated large-scale BOLD activations and corresponding behavioral preference via combining (1) the cell-type specific opto-fMRI on BF VGLUT2, ChAT, PV and SOM neurons, (2) the BF cell-type specific anatomical projections and (3) optogenetic free-moving behavioral test. Firstly, through our systematically optimized awake mouse opto-fMRI setup, we found distinct global BOLD responses evoked by the cell-type specific activations of BF neurons. Then, combining the BF cell-type specific anatomical projections, we found BF-originated low dimensional structural networks significantly contributed to cell-type specific opto-fMRI activations. Furthermore, we revealed that activation of BF excitatory (VGLUT2 and ChAT) or inhibitory (PV and SOM) neurons induced externally or internally oriented behavioral preference, respectively. Importantly, we developed a model to link the BF-modulated BOLD activations inside the magnet and behavioral preference outside the magnet, and decoded the global patterns of internally and externally oriented behaviors. In conclusion, we revealed both cholinergic and non-cholinergic neurons modulated global functional networks with corresponding internally and externally oriented behavioral preferences, and provided a new perspective to link the BOLD activations to behavioral relevance.

# Results

## Optogenetic stimulations of BF neurons evoke distinct cell-type specific BOLD activations

We combined Cre-dependent virus (AAV2/9-hSyn-DIO-ChrimsomR-mCheery-WPRE-pA) and VGLUT2-, ChAT-, PV- and SOM-Cre mice to express of ChrimsomR in glutamatergic, cholinergic, PV and SOM GABAergic neurons in BF (Fig. 1A and S1). To accommodate the limited space in cryogenic coil, flexible PMMA optical fibers were used in combination with our previous awake mouse fMRI[26–28] to establish the awake mouse opto-fMRI setup (Fig. 1A-D). The biband EPI pulse sequence[28] was employed to achieve faster acquisition (TR = 500 ms) while maintaining whole brain coverage (in-plane resolution = 150 $\mu m^2$ with 38 axial slices).

Using our optimized awake mouse opto-fMRI setup and standardized data processing protocol (Fig.1A and Fig. S2)[26–29], we observed robust and cell-type specific large-scale BOLD fMRI activations (Fig. 1E and Fig. S3). Activation of VGLUT2 neurons in the BF elicited the strongest and most widespread BOLD activations throughout the brain among all four cell types (Fig. 1E, upper panel). Activation of ChAT neurons resulted in positive activations across extensive cortical and subcortical regions, including the prefrontal cortex (PFC), ACA, RSP, orbital (ORB), visual (VIS), auditory (AUD), entorhinal (ENT) areas as well as a large proportion of striatum and thalamus (Fig. 1E, upper middle panel). In PV-Cre group, ACA showed significant positive activation (Fig.1E, lower middle panel). In SOM-Cre group, significant positive activations were observed in ACA, striatum and anterior thalamus (Fig. 1E, lower panel). Interestingly, the VGLUT2- and ChAT-Cre groups exhibited significant negative activation constrain within the motor (Mot) and somatosensory (SS) areas, while the PV-cre group showed negative activation within VIS.

Notably, we consistently observed positive activations in the DMN-like regions (Fig.1E and Fig. 2A-C). Importantly, BF PV neurons exhibited the highest specificity for DMN-like activations (Fig. 2D and Fig. S5) rather than VGLUT2 neurons. Such a phenomenon was consistent with the previous finding in rats that optogenetic stimulation of BF PV neurons activated the DMN-like network and associated behaviors[25].

138 **BF-originated low dimensional structural networks significantly**
139 **contribute to cell-type specific opto-fMRI activations.**

140 To investigate whether the functional activation was directly governed by
141 corresponding anatomical projections from BF neurons, we adopted the previously
142 published anterograde axon tracing data[4] and registered to our standard MRI space (Fig.
143 3A and 3B). Cholinergic BF neurons displayed widely spread projections to the cortex,
144 while the non-cholinergic neurons mainly innervated subcortical brain regions and had
145 limited projections to most parts of the cortex (Fig. 3B). To evaluate the structural-functional
146 correspondence across BF cell types, we calculated the spatial correlation between
147 functional activations (Fig. 1E and Fig. 2A) and anatomical outputs (Fig. 3B). Weak
148 structural-functional correspondence was found for all BF cell types (Fig. 3C, brown arrows
149 and Fig. S6-7), suggesting direct anatomical projections weakly contributed to opto-fMRI
150 activation patterns.

151 One potential contributor to the functional responses was secondary projections of the
152 regions that receive direct projections from BF neurons (Fig. 4A). To examine such a
153 hypothesis, we generated the cell-type specific BF secondary projection matrix by spatial
154 weighting the voxel-wise whole-brain mesoscopic connectivity matrix[30,31] based on the BF
155 direct projections (Fig. 4B & Fig.S8). We concatenated secondary projections from four
156 types of BF neurons to cover all projections originating from BF, including those from local
157 interaction of BF cell types. Then, the concatenated secondary projections were further
158 decomposed using the non-negative matrix factorization (NMF) analysis (Fig. 4B & Fig.
159 S8). One significant advantage of NMF over other dimensionality reduction techniques is
160 its ability to ensure that all elements in the decomposed low-rank matrix are non-negative,
161 which is crucial for interpreting both NMF components and associated weights as actual
162 network activity.

163 Subsequently, we identified six low-dimensional NMF components that were
164 predominantly composed of brain stem, olfactory, DMN-like, visual, hippocampus and
165 sensorimotor network (Fig. 4C & Fig.S9), respectively. We observed that low-dimensional
166 structural networks exhibited a higher explained variance in cell-type specific opto-fMRI
167 responses compared to the direct projections (Fig. 4D-E and Fig. S10), indicating their

168 dominant effect on cerebral dynamics. The scaling coefficients of NMF components were
169 then defined as optimal feature vectors, representing the engagement levels of NMF
170 components under optogenetic activation of BF neurons (Fig. 4F). Therefore, these
171 findings provide evidence that BF originated low dimensional structural networks
172 significantly contributed to cell-type specific opto-fMRI activations.

173 **Inhibitory (PV and SOM) or excitatory (VGLUT2 and ChAT) neurons in BF**
174 **support internally or externally oriented behaviors respectively.**

175 We further investigate whether cell-type specific modulation of BF exerted an impact
176 on mouse internally and externally oriented behaviors. The behavioral test was conducted
177 in the arena under the same optogenetic stimulation paradigms as in the fMRI experiments
178 to examine the locomotion speed, quiet wakefulness, grooming and object explorations
179 (Fig. 5A-C). The VGLUT2-Cre group exhibited a significantly higher locomotion speed (Fig.
180 5D), which was consistent with the wakefulness and avoidance behavior-promoting effect
181 of BF VGLUT2 neurons[3,15,16]. The ChAT-Cre group demonstrated significantly higher novel
182 object explorations (Fig. 5E), which is consistent with the involvement of cholinergic
183 systems in attention, learning, and memory[11,12]. There were no discernible differences in
184 familiar object exploration among the groups (Fig. S11). Moreover, optogenetic stimulation
185 of BF PV neurons resulted in the highest DMN-associated behavior, specifically grooming
186 (Fig. 5G), which is consistent with the previous study in rats[25]. SOM-Cre group exhibited a
187 greater duration of quiet wakefulness in comparison to other subpopulations (Fig. 5F), in
188 line with the sleep-promoting[3] and locomotion-inhibiting effects[32] of BF SOM neurons.

189 To further investigate the preference of BF cell types in mouse behaviors, we
190 normalized behavioral performances by dividing each maximum (Fig. 5H). Subsequently,
191 we found activated VGLUT2 and ChAT neurons preferentially drove externally oriented
192 behaviors such as locomotion and novel object exploration, while activated PV and SOM
193 neurons drove internally oriented behaviors like grooming and quiet wakefulness (Fig. 5H).

194 **Decoding model links BF-modulated BOLD activations and internally and**
195 **externally oriented behavioral preference**

196 As the same optogenetic stimulation paradigm was applied in opto-fMRI and
197 behavioral test, we hypothesized that cell-type-specific activation maps and behavior-
198 related cerebral patterns share common low-dimensional (NMF) space (Fig. 6A). Therefore,
199 we constructed a decoding model (Fig. 6B) to predict the behavior related global patterns,
200 based on the feature vectors of BOLD activations (Fig. 6C) and behavioral performance
201 (Fig. 5G-H). The model's regression coefficients were identified as behavior-related feature
202 vectors, representing predicted cerebral patterns of each behavior in the NMF space (Fig.
203 6D). The minimal deviation angle (Fig. 6E, red shadow) between feature vectors of BOLD
204 activations (Fig. 6C) and behaviors (Fig. 6D) indicated the behavioral preference, e.g., the
205 feature vector of VGLUT2 group had minimal deviation angle with that of locomotion (Fig.
206 6E), corresponding to its preference on locomotion (Fig. 5D). The significantly negative
207 correlations between the deviation angles and empirical behavioral results (Fig. 6F) further
208 suggested that low dimensional network organization supported the behavioral preference
209 of BF cell types.

210 Based on the behavior-related feature vectors (Fig. 6D) and the spatial patterns of
211 NMF components (Fig. 3C), we further predicted the cerebral responses of behaviors (Fig.
212 6G). Interestingly, the predicted global pattern of grooming showed opposing patterns
213 between intrinsic networks (i.e., DMN-like network) and extrinsic networks (e.g., salience
214 network) (Fig. 6G, lower middle panel), which was consistent with previous findings in
215 rats[33] and human[34–37]. The predicted global pattern of quiet wakefulness (Fig. 6G, lower
216 panel) exhibited high spatial similarity to that of grooming, and both of these were opposing
217 to that of locomotion (Fig. 6G, upper panel). Moreover, the predicted global pattern of novel
218 exploration (Fig. 6G, upper middle panel) exhibited robust positive responses in the
219 prefrontal cortex and hippocampus, consistent with previous evidence of cholinergic
220 innervation to these regions involved in novelty preference[38–40].

221 To verify the predicted spatial patterns of mouse behaviors, we first conducted the
222 awake mouse fMRI scanning with simultaneous behavioral monitoring using two
223 customized MR-compatible cameras (Fig. 7A). We observed apparent grooming behavior

during the scanning (Fig. 7B) and corresponding functional activations (Fig. 7C). Significant positive correlation between the empirical (Fig. 7C) and predicted (Fig. 6G) spatial maps indicated the validity of predicted global patterns of mouse behaviors. We further conducted another verifying experiment with simultaneous calcium fiber photometry in ACA, primary motor area (MOp), and entorhinal cortex (ENT) during free-moving behaviors (Fig. 7E-F). We found a notable positive correlation between the predicted spatial weights and neural activities (Fig. 7G) during quiet wakefulness, grooming, and novel object exploration. The negative correlation during locomotion was unexpected but somewhat reasonable, as the locomotion consistently elicits widespread activation and can potentially confound the analysis of other behaviors[41]. Thus, the above two verifying experiments highlighted the reliability of our decoding model and the resulting predicted global patterns of mouse behaviors. Therefore, our results provided a framework for behavioral research through the lens of cerebral network basis, linking the BF-modulated BOLD activations to the internally and externally oriented behavioral preference.

# Discussion

The functional roles of BF cholinergic and non-cholinergic neurons, from large-scale functional networks to behaviors, remain elusive. We first demonstrated cell-type specific whole-brain responses and corresponding internally and externally oriented behavioral preference induced by optogenetic activation of four BF neuron types. Subsequently, we developed a decoding model to link the BF-modulated BOLD activations and behavioral preference based on the organization of a low-dimensional cerebral network. Ultimately, we predicted the global patterns of mouse behavioral preference via our model, which were verified by two different experiments, i.e., (1) awake mouse fMRI with simultaneous grooming monitoring and (2) calcium fiber photometry during free-moving behavior test. In summary, our results demonstrated that both cholinergic and non-cholinergic BF neurons modulate cerebral functional networks and corresponding internally and externally oriented behavioral preference. Our results also provided a framework for investigating animal's behaviors in the whole brain view.

It is not trivial to acquire high-quality opto-fMRI data in mice, with many limiting factors such as anesthesia, low SNR, and image artifacts caused by fiber implants. So far, most previous opto-fMRI studies in rodents have been conducted under anesthesia[42–49], with only a few exceptions[50–52]. To avoid the confounding factors of various anesthesia methods[53,54], we established the awake opto-fMRI setup based on our extensive experience in awake mouse fMRI[26–29]. Furthermore, a multiband EPI pulse sequence was employed to acquire functional images to achieve faster acquisition while maintaining whole brain coverage[28]. To take advantage of the high SNR provided by the cryogenic RF (radio frequency) coil, a flexible PMMA optic fiber implant was used to accommodate the limited space of the cryogenic coil (Fig. 1B). Importantly, PMMA has similar magnetic susceptibility to that of the brain tissue[55] thus reduced imaging artifacts caused by fiber implantation (Fig. 1C). In conclusion, we have optimized the setup for awake mice opto-fMRI systematically to acquire high-quality opto-fMRI data.

With the optimized approach described above, we revealed cell-type specific whole-brain responses under optogenetic activation of BF neurons. The most strong and

widespread BOLD responses (Fig. 1E, upper panel) and corresponding highest locomotion speed (Fig. 5D) of BF VGLUT2 group possibly attribute to the promoting wakefulness and avoidance behavior effects of BF VGLUT2 neurons[3,14,15]. The activation of the PFC, Mot, SS, AUD, VIS, and striatum (Fig. 1E, upper panel) and corresponding highest novel object exploration (Fig. 5E) of the ChAT group were consistent with the BF cholinergic neuron involved circuits that modulate recognition memory, sensory perception and attention regulation[38,40,56–59]. The higher quiet wakefulness (Fig. 5F) of SOM group may attribute to the sleep-promoting[3] and locomotion-inhibiting effects[32] of BF SOM neurons. Importantly, PV group showed positive activation mainly within DMN-like network, resulting the highest specificity for DMN-like activations of PV group than other groups (Fig.1E, lower middle panel and Fig. 2D), along with the corresponding highest grooming (Fig. 5G). The above results were consistent with previous work on BF PV neurons' modulation on DMN-like networks and internally oriented behaviors[25]. Interestingly, we consistently observed positive activations in the DMN-like regions (Fig. 1E and Fig. 2) under the activation of all four BF neuron types, indicating the complex yet robust interaction between BF and cortical DMN-like network. It also supports the notion that BF may be part of a subcortical DMN network[24,25,35,60–62]. Therefore, the current study provided a more complete perspective for whole-brain functional responses and corresponding behavioral preference from activations of four BF neuron types.

It is well known that the primary anatomical projections are key regulators of functional dynamics. Interestingly, we found weak structural-functional correspondence between BF cell-type specific anatomical projections and functional activations. Such phenomenon was consistent with the finding that functional connectivity originated from dopamine neurons in the ventral tegmental area[46] and serotonin neurons in the dorsal raphe[42] were uncoupled with corresponding dopaminergic and serotoninergic neuron projection density, respectively. Our results demonstrated the low dimensional structural networks decomposed from BF-originated secondary projections significantly contributed to the cell-type specific BOLD activations. As previous studies demonstrated that the low dimensional structural networks served as the backbone of functional dynamics and cognitions in human or marmoset brain[63,64], our finding suggested the dominating effects of low

300 dimensional structural networks on functional activations are markedly consistent across
301 species.

302 However, a framework to systematically establish the link among the cell-type specific
303 BF modulations, global structural networks, and behavioral preference is lacking. Thus,
304 our study built a decoding model to link the BF-modulated global activation patterns and
305 the behavioral preference in a low dimensional network space (Fig.6). After projecting high
306 dimensional BOLD activations into low dimensional space spanned by structural networks,
307 i.e., NMF components (Fig. 4C), the dimension of resulting features, i.e., weights of NMF
308 components (Fig. 4F and 6C), were much closer to the dimension of mouse behaviors.
309 Using the low dimensional features as model inputs highly improved the computational
310 efficiency. More importantly, such a strategy enhanced the feasibility of capturing
311 discriminative features from BF-modulated BOLD activation patterns, which were
312 subsequently used to model the corresponding behavioral preference. Also, our BF cell-
313 type specific opto-fMRI, including manipulation on four neuron types instead of one[22],
314 provided more complete and informative BOLD features as the model inputs, improving
315 the robustness of our decoding model.

316 Interestingly, our modeling approach provided a general methodology to explore the
317 global patterns of behaviors. Based on the decoding model, we back-reconstructed the
318 global patterns of mouse behaviors, such as quiet wakefulness and grooming (Fig.6 B&G).
319 Thus, the predicted global patterns offered potential 'reference templates', similar to the
320 "arousal template"[65], and could be used to infer the behavioral occurrence through the
321 spatial correlation between the template and the empirical imaging data[18,65]. Nevertheless,
322 it is difficult to experimentally verify the predicted global patterns (Fig. 6G) in the MRI
323 scanner. Thus, we further modified our awake mouse fMRI setup to allow the animal's
324 forelimbs to groom during the fMRI scanning (Fig. 7B), and obtained the empirical
325 grooming evoked BOLD activations (Fig. 7C). The significant correlation between empirical
326 and predicted grooming patterns (Fig. 7D) provided the experimental validation for our
327 decoding model. Interestingly, the grooming pattern with activations in DMN regions and
328 de-activations in extrinsic networks (e.g., salience network) was in line with BOLD
329 responses during internally focused cognitive state in the previous human studies[34–37].

330 Together, these results suggested the reliability of our modeling approach, which could be
331 further used in inferring the global patterns of behaviors in future imaging studies.
332 Previous human imaging studies[34–37] revealed significant DMN activation and dorsal
333 attention network suppression under internally focused conditions. Such a phenomenon
334 was in accordance with our empirical groom activations (Fig.7C), suggesting the cross-
335 species consistency of the anti-correlated relationship between intrinsic and extrinsic
336 networks[66]. During the external task condition, the BF and DMN were deactivated together
337 in human fMRI studies[34,35,67]. The BF's prominent structural connectivity with DMN-like
338 cortical regions has been suggested to parallel its known modulatory projections involving
339 cholinergic, GABAergic, and glutamatergic systems[4]. In our study, we revealed the highest
340 specificity for the DMN activations with corresponding grooming preference under the
341 optogenetic activations of BF PV neurons (Fig.2 & 4). Such results agreed with previous
342 studies that projections of BF PV neurons have been specifically linked to the control of
343 DMN state transitions in rats[25,33]. Therefore, we confirmed the BF PV neurons on the DMN
344 activity during the internally oriented behaviors.
345 An important limitation in our model was the assumption that the same optogenetic
346 stimulation paradigm induced a similar global response inside and outside the magnet.
347 Naturally, the brain state of the mouse was undoubtedly different in those two environments.
348 However, it is not unreasonable to assume that the strong cerebral responses were more
349 dominated by the optogenetic stimulations than the environment. Moreover, our empirical
350 evidence provided experimental support for the validity of our modeling approach (Fig. 7).
351 Another limitation was the lack of recording the natural activity of cell-type specific BF
352 neurons during various behaviors, such as grooming, for better confirmation of different BF
353 neuron types associated with behavioral preferences. Besides, the current study only
354 examined the cell-type specific effects of BF neuron activation. Future investigations
355 should incorporate cell-type specific inhibition of BF neurons for a more complete view.
356 Last but not least, the complex interactions among BF neuron types[3] were not specifically
357 considered in the current model, and further biological modeling incorporating these local
358 connections could be conducted in the future. Nevertheless, our concatenated secondary
359 projections covered all potential outputs originating from BF regardless of the local

interactions within BF. Thus, our results were unlikely to be affected by the complex interactions among BF neuron types.

# Methods

## Animals

All animal experiments were approved by the Animal Care and Use Committee of the Institute of Neuroscience, Chinese Academy of Sciences, Shanghai, China. Experiments were conducted with mice at 8-10 weeks of ages, weighted 18-30 g. Number of mice in each experiment was listed in Table1. No statistical methods were used to predetermine sample sizes but our sample size is similar to previous publications[51,68]. Wild-type mice were purchased from institute-approved vendors (Shanghai Laboratory Animal Center, or LingChang Experiment Animal Co., China), and ChAT-IRES-Cre, VGLUT2-IRES-Cre, PV-IRES-Cre and SOM-IRES-Cre mice (Jackson stock #: 006410, 016963, 008069 and 013044 respectively) were obtained from Jackson Laboratory. Mice were group-housed (5–6/cage) under a 12-h light/dark cycle (light on from 7 a.m. to 7 p.m.) with food and water *ad libitum*.

Table 1 Summary of Number of mice used in each experiment.

| | | ChAT-Cre | PV-Cre | SOM-Cre | VGLUT2-Cre | Wild-type |
|---|---|---|---|---|---|---|
| optogenetic stimulations with | fMRI imaging | 8 | 11 | 10 | 8 | 7 |
| | free-moving behavioral test | 7 | 8 | 7 | 7 | 7 |
| Verifying experiment 1: fMRI imaging with behavioral monitoring | | - | - | - | - | 11 |
| Verifying experiment 2: Fiber photometry | | - | - | - | - | 6 |
| Comparing artifacts of PMMA and $SiO_2$ optical fiber | | | | | | 5 |

## Stereotaxic surgeries

All stereotaxic surgeries were conducted under isoflurane anesthesia (5% for induction and 1-1.5% for maintenance), and animals were placed on a stereotaxic frame with a heating pad (mouseSTAT, Kent scientific cooperation). A midline sagittal incision

385 was made along the scalp to expose the skull. Two craniotomies (~0.4 mm in diameter)
386 were made on top of bilateral BF (AP 0 mm, ML ±1.3 mm), targeting the intermediate
387 portion of the BF, including the horizontal limb of the diagonal band of Broca (HDB),
388 magnocellular preoptic nucleus (MCPO) and substantia innominate (SI). AAV2/9-hSyn-
389 DIO-ChrimsonR-mCherry-WPRE-hGH pA (Titer: $4.76 \times 10^{12}$ v.g. /mL; BrainVTA Co., China)
390 was injected into each side of BF(AP 0 mm, ML ±1.3 mm, DV -5.0 mm from dura) utilizing
391 Nanoject III (Drummond Scientific) via a glass pipette (1 nL/s, 20 nL/cycle, inter-cycle
392 interval 10 s, total 20 cycles and 0.4 μL). After each injection, the needle was slowly pulled
393 up following a 10-min waiting period to prevent backflow. Then scalp was sutured, and
394 mouse was placed in a postoperative incubator for anesthesia recovery.

395 Optical fiber and head holder implantation for awake optogenetic fMRI were performed
396 two weeks after virus injection. Head holder design and the surgical procedure were
397 modified from our previous study[26]. The scalp over the skull was removed, and then the
398 periosteum was removed with cotton swabs dipped in 3 % hydrogen peroxide. The tissue
399 covering the skull posterior to the lambda point was also removed for firmer fixation of the
400 head post. Then, the exposed skull was cleaned by saline. After drying the surface of skull,
401 a coat of self-etch adhesive (3 M ESPE Adper Easy One) was applied followed by light
402 curing.

403 To reduce imaging artifacts caused by fiber implantation and also accommodate the
404 limited space of the cryogenic RF coil, we chose flexible fiber optic implants (200 μm in
405 diameter; NA 0.5; Inper Co., China) made of poly-methylmethacrylate (PMMA) which has
406 similar magnetic susceptibility to the brain tissue/water[55]. Two craniotomies (~0.4 mm in
407 diameter) were made on top of bilateral BF and the PMMA optic fibers were inserted into
408 bilateral BF (AP 0 mm, ML ±1.3 mm, DV -4.8 mm from dura). After draining the overflow of
409 liquid from the craniotomy with dust-free paper, the light curing flowable dental resin was
410 applied and cured with blue light for 20 s to fix the optic cannula to skull. After adhering the
411 skin surrounding the exposed skull with tissue adhesive, the dental resin was applied on
412 the occipital bone, and a custom-made MRI-compatible head holder was place closely on
413 the same place. Then, the flexible PMMA optic fibers were bent and fixed on the surface
414 of skull and head holder with dental resin (Fig. 1B). Finally, other exposed regions of the

skull was covered with a thick smooth layer of dental cement. After surgery, the mice were placed in a postoperative incubator for anesthesia recovery.

## Habituation for awake mouse optogenetic fMRI (opto-fMRI)

After 1-week recovery from the fiber and head holder implantation, mice were habituated for awake fMRI for seven days (Fig. 1A). Mice were head-fixed on an animal bed with the recorded acoustic MRI scanning noise, following a previously described habituation paradigm [28]. The detailed schedule was listed in Table 2. No reward was given during and after the habituation training.

Table 2 Summary of habituation schedules for awake mouse ofMRI

| | **Day1** | **Day2** | **Day3** | **Day4** | **Day5** | **Day6** | **Day7** |
|---|---|---|---|---|---|---|---|
| Duration of Habituation | 60 min | 60 min | 60 min | 60 min | 60 min | 60 min | 60 min |
| Acoustic Noise | - | 60 dB | 60 dB | 90 dB | 90 dB | 110 dB | 110 dB |

"–" denote absence.

## Optogenetic fMRI acquisition

All MRI data were acquired with a Bruker BioSpec scanner (9.4T/30cm, Bruker, Billerica, USA, ParaVision 6). An 86 mm volume coil was used for transmission and a 4-channel cryogenic phased array mouse head coil (Bruker) was used for receiving. A thick layer of Kwik-cast was applied smoothly over the mouse skull immediately before the MRI scanning to reduce distortion caused by air. The mouse was first secured in the animal bed without any anesthesia. Light delivery systems were kept outside the magnet and 7 m fiber optic patch cable (200 μm in diameter; NA 0.5; Doric Lens) were used to deliver light into the bore of the scanner. Optical patch cable was attached to the implanted optic fiber using a zirconia sleeve (Thorlabs). Then the mouse was placed inside the MRI scanner. A T2-weighted structural image was acquired for co-registration with following parameters: TR = 3400 ms, TE = 33 ms, field of view = 16 × 16 $mm^2$, matrix size = 256 × 256, slice thickness = 0.5 mm, 30 axial slices, RARE factor = 8, and number of averages = 2. After field map based local shimming within the mouse brain, Biband-EPI was acquired using

440 the multiband EPI sequence [28] with the following parameters: TR = 500 ms, TE = 15 ms,
441 flip angle = 38.8°, bandwidth = 300 kHz, field of view = 15 × 10.5 $mm^2$, matrix size = 100 ×
442 70, nominal slice thickness = 0.48 mm (slice thickness 0.4 mm with a gap of 0.08 mm),
443 674 or 737 volumes (scan 1-3: 674 volumes and scan 4-6: 737 volumes), and 38 axial
444 slices per scan. During the Biband-EPI scanning, an Arduino Uno board
445 (https://www.arduino.cc/) was use to synchronize the scanner trigger and the lasers for
446 optogenetic stimulations. Red light (10 Hz, 5% duty cycle) was delivered to the bilateral BF
447 utilizing 638 nm laser (Shanghai Laser & Optics Century Co., Ltd.), and the power at the
448 fiber tip was 5 mW. The overall stimulation setup was shown in Fig. 1D. For each EPI run,
449 28 stimuli were delivered with durations of 0.5 s or 2 s, and a random inter-trial-interval
450 time of 15 +/- 5 s.

451 **Simultaneous behavioral monitoring and fMRI acquisition**

452 For the awake mouse fMRI with simultaneous behavior monitoring, a similar imaging
453 protocol was used as mentioned above, with the following difference: Biband-EPI TR = 750
454 ms, flip angle = 46.6° and 10000 volumes per scan. In addition, two custom-made MR-
455 compatible video cameras (sampling rate of 25 fps, 1080 × 980 pixels) was placed inside
456 the bore to record the spontaneous behaviors, e.g., grooming and body motion, which were
457 later used to estimate the grooming evoked BOLD activations.

458 **fMRI data processing**

459 After the image format conversion, the mouse brain was extracted manually utilizing
460 ITK-SNAP (http://www.itksnap.org/). All subsequent procedures were performed utilizing
461 custom scripts in MATLAB 2020a (MathWorks, Natick, MA) and SPM12
462 (http://www.fil.ion.ucl.ac.uk/spm/). Images of each scan were registered to the scan-
463 specific structural image utilizing rigid body transformation, and the scan-specific structure
464 image was then nonlinearly transformed to the 3D Allen Mouse Brain Common Coordinate
465 Framework, v3 (CCFv3, http://atlas.brain-map.org/) for group analysis Then, a light spatial
466 smoothing (0.4 mm isotropic Gaussian kernel) was performed. Furthermore, BOLD signals
467 were regressed by “6 rp + 6 Δrp + 10 PCs” nuisance signals to minimize the effects of

468 scanner drift, motion and other non-neural physiological noises (Fig. S2), adopted from our
469 previous study [26]. “6 rp + 6 Δrp” nuisance signals represented 6 head motion parameters
470 and their 1st order first derivatives, and “10 PCs” were the first 10 principal components
471 from the BOLD signals of non-brain tissue, e.g., the muscles. The Pearson’s correlation
472 coefficients between the frame-wise displacement (FD) and DVARS (D referring to
473 temporal derivative of time courses, VARS referring to RMS variance over voxels) were
474 calculated to quantitatively evaluate to what extent the motion related signal was reduced
475 by given regressors [29].

## 476 General linear model of cell-type specific optogenetic stimulations and 477 spontaneous behaviors

478 GLM based statistical analysis was conducted utilizing the awake mouse-specific
479 hemodynamic response function (HRF) from our previous study [26]. Standard first level
480 analysis was done for individual EPI scans. For the awake mouse fMRI experiment with
481 optogenetic stimulations, the period of optogenetic stimulations was set as the predictors.
482 Also, a flexible factorial model including cell-type specific optogenetic stimulations and
483 individual mouse (as random effect) was conducted for second level analysis to generate
484 the activation maps and then thresholded with FDR corrected $p < 0.05$.

485 For the awake mouse fMRI experiment with simultaneous behavior monitoring, the
486 behaviors (e.g., grooming and body motion) were used as the predictors and thus the
487 remaining period was used implicitly as the baseline. A one-sample t-test was conducted
488 for second level analysis to generate the activation maps with FDR corrected $p < 0.05$.

## 489 Specificity of DMN-like activations driven by BF neurons

490 The ICA-based functional networks were adopted from a previous study[69], in which
491 they identified macro-communities to spatially encompass six macroscopic networks of the
492 mouse cerebrum. Briefly, the mouse resting state (rs-)fMRI dataset was fed into MELODIC
493 (Multivariate Exploratory Linear Optimized Decomposition of Independent Components) [70]
494 to perform within-subject spatial ICA. Using preset 30 components and the ICA-FIX pre-
495 processing pipeline, 23 out of 30 components were detected in meaningful anatomical

496 regions of the mouse brain and considered as rs-fMRI functional networks. Then,
497 hierarchical network analysis was performed based on total correlation matrices of the 23
498 group ICA signal components and subsequently merged the group ICA components into
499 six cerebral clusters, i.e., DMN-like (Fig. 2B), somatosensory, sensory, hippocampus, basal
500 ganglia and olfactory networks (Fig. S4). The proportion of significantly activated voxels
501 that overlapped with ICA-based functional networks (Fig. 2B and Fig. S4) was calculated
502 with opto-fMRI responses were thresholded at FDR-corrected $p < 0.05$, while ICA-based
503 functional networks were thresholded at $z > 3$.

504 Receiver operating characteristic (ROC) curves were computed to evaluate the
505 specificity of opto-fMRI activations (Fig. 1E and Fig. 2A) on mouse ICA-based functional
506 networks (Fig. 2B and Fig. S4A)[71]. Briefly, functional networks and opto-fMRI responses
507 were normalized between 0 and 1, and were binarized using a series of 100 thresholds to
508 keep the 0-100% of activations, respectively. The resulting binary functional networks and
509 opto-fMRI responses were compared using the ROC analysis with the corresponding
510 functional network, i.e., DMN-like network, as the ground truth. The true positive and false
511 positive rate vectors were plotted against each other and the resulting area under the curve
512 (AUC) was used as the measurement of the specificity of opto-fMRI activations on mouse
513 functional networks. The AUC results were then compared against a null distribution of the
514 same datasets using the permutation test with 1000 times shuffling of the cell-type specific
515 opto-fMRI responses.

## 516 Anterograde axon tracing from BF neurons

517 The whole-brain axonal projections data from the four BF cell types is modified from
518 our previous study[4]. Briefly, ChAT-Cre, PV-Cre, SOM-Cre or VGLUT2-Cre mice were
519 anesthetized with ~1.5% isoflurane in oxygen, 300-400 nL output tracing vector (AAV2-
520 EF1a-FLEX-mCherry, titer: ~$10^{12}$ gc/mL) was inject into the right BF. Two to three weeks
521 after AAV injection, mice were deeply anesthetized with isoflurane and immediately
522 perfused intracardially with PBS followed by 4% PFA. Brain was removed and post-fixed
523 in 4% PFA in PBS at 4 ℃ overnight, dehydrated in 30% sucrose in PBS for 48 hr, embedded
524 in Tissue Freezing Medium, cut in 30 or 50 μm coronal sections and mounted with

525 VECTASHIELD antifade mounting medium with DAPI. All sections were imaged utilizing
526 20X/0.75 objective in a high-throughput slide scanner for further 3D reconstruction and
527 quantification. The digitized analysis was performed with a software package which
528 consists of three modules: image registration, signal detection, and quantification.

## 529 Voxel-wise whole-brain mesoscopic structural connectivity

530 Whole-brain structural connectivity was obtained from the Allen Mouse Brain
531 Connectivity Atlas (http://connectivity.brain-map.org/), which was based on 428 viral
532 microinjection experiments in C57BL/6J male mice. Briefly, adeno-associated viral
533 anterograde tracers, containing genes encoding for enhanced green fluorescent protein,
534 were sterotactically injected at different sites in mice. After the injection, 2 weeks were
535 allowed for the protein expression before the animals were killed, the brain was extracted,
536 sectioned, imaged with two-photon microscope, reconstructed into 3D fluorescence maps,
537 and transformed into a common reference space [72]. Then, the connectome data were
538 aggregated according to a voxel-wise interpolation model [31], modeling the connectivity at
539 each voxel as a radial basis kernel-weighted average of the projection patterns of nearby
540 injections. Thus, a high-resolution mouse brain connectome (100 $\mu m^3$) was estimated
541 according to a Voronoi diagram based on Euclidean distance between neighboring voxels
542 [31]. The Voronoi-based resampling allowed us to spatially weight voxels with respect to
543 neighboring areas, and preserve the intrinsic architectural foundation of the connectome.
544 Finally, fiber tracts and ventricular spaces were filtered out, yielding a final weighted and
545 directed 15,314 × 15,314 matrix composed of 0.027 $mm^3$ aggregate Voronoi voxels.
546 Notably, the structural connectivity matrix was transformed by the logarithm operation
547 similar to our previous study [63].

## 548 Non-negative matrix factorization

549 To further investigate how the BF modulated global organizations of mouse cerebral
550 functional networks, we firstly concatenated the four cell-type secondary projections from
551 BF neurons (Fig. S8), in which the secondary projections was adopted from source-
552 weighted whole-brain mesoscopic structural connectivity by cell-type output from BF

553 neurons, thus resulting a 15,314 × 61,256 connectivity matrix (Fig. S8). Considering the
554 bilateral optogenetic stimulations on BF neurons, we averaged the connectivity strengths
555 from ipsilateral and contralateral hemispheres for both cell-type specific output from BF
556 (Fig. 4B) and whole-brain mesoscopic structural connectivity matrix. Then, the non-
557 negative matrix factorization (NMF) was performed on the resulting secondary connectivity
558 matrix (15,314 × 61,256, Fig. 4B). The spatial NMF components ($W_{p_0 \times 15,314}$) were back-
559 projected to whole-brain BOLD signals to reconstruct the time course of each component
560 ($S_{t \times p_0}$) for each individual EPI scan. NMF was chosen over other dimensional reduction
561 methods, e.g., PCA or ICA, because it enhances the interpretability of the resulting low
562 dimensional components. To estimate the appropriate dimensionality of the NMF analysis,
563 we calculated the mean cophenetic coefficients following the NMF decomposition (a
564 measure of the optimal number of subgroups in the connectivity matrix), and found the
565 maximum coefficient in the top 6 components (Fig. S9A). Thus, we chose the top 6 NMF
566 components in all following analysis.

567 **Optogenetic free-moving behavioral test**

568 Free-moving optogenetic behavioral test was performed in a 40 × 40 × 40 $cm^3$ arena
569 (Fig.5A). To keep the behavioral testing condition similar to the MRI experiment, the phase
570 of familiarization was set to 30 min with two familiar objects in two corners of arena. Then,
571 one of the familiar objects was replaced by a novel one (different shape, texture, size, and
572 color). The same optogenetic stimulations as in MRI were then delivered to the bilateral
573 BF immediately (Fig.5B). Animal behaviors were recorded utilizing a video camera (25 fps,
574 1080 × 980 pixels), which was positioned 50 cm above the center of the arena floor.

575 To analyze the recorded video, a set of behaviors including (1) locomotion speed, (2)
576 quiet wakefulness, (3) grooming, (4-5) familiar and novel object explorations were recorded.
577 Object exploration was defined as the mouse's nose was < 1 cm from the object and the
578 dwell time was < 4 s. Locomotion was labelled when the speed was > 2 cm/s excluded the
579 period of object explorations. Moreover, we fitted the outline of mouse body by an ellipse
580 and used the major ($a$) and minor ($b$) axes of the ellipse to distinguish the grooming and
581 quiet wakefulness. The behavioral state of grooming was termed when the mouse was in

a quasi-stationary condition (speed < 2 cm/s) and the outline of mouse body was sub-rounded (i.e., $a - b$ > 2 cm). The remaining quasi-stationary behavior (speed < 2 cm/s, $a - b$ < 2 cm) was defined as the quiet wakefulness with short periods (dwell time < 5 s) excluded. Durations of the five types of behaviors were scored.

## Decoding the global patterns of mouse behaviors

A general decoding model was used to predict the cerebral responses of mouse behaviors (Fig. 6B). As the optogentic fMRI and free-moving behavioral tests were conducted in different days, we divided the total behavior length into 6 runs for each mouse, keeping temporal alignment with the order of fMRI scanning. Then, we averaged both the weights of NMF components and behavioral performances across mouse individuals, and only considered the group-wise behavioral variability under optogenetic stimulations on cell-type specific neurons. The resulting cell-type specific BOLD weights of NMF components ($W_{4\times6\times6}$) were set as the model predictors (4 cell-types, 6 runs and 6 NMF components), and the cell-type specific behavioral performances ($Y_{4\times6}$) were termed as the model output.

We randomly divided 6 runs into two groups to generate encode and decode datasets respectively, and repeated 20 times for traversing all random conditions, i.e., choose 3 runs as encoding dataset from all 6 runs. The regularization penalty was estimated on the encoding dataset utilizing marginal maximum likelihood estimation with minor modifications that reduced numerical instability for large regularization parameters. To avoid over fitting, ridge regression was chosen over other regularization methods (e.g., LASSO or elastic net) because a sparseness prior would isolate the best contributing model variables and completely reject variables which have slightly less informative. Regression coefficients ($\beta_0$, $\beta_1$, $\beta_2, \beta_3$, $\beta_4$, $\beta_5$ and $\beta_6$) were termed as the representative vector $[\beta_1, \beta_2, \beta_3, \beta_4, \beta_5, \beta_6]$ for each mouse behavior in NMF space, and further used to construct corresponding spatial patterns ($[\beta_1, \beta_2, \beta_3, \beta_4, \beta_5, \beta_6] \cdot W_{6\times15314}$) by multiplying the spatial NMF components ($W_{p_0\times15,314}$ and $p_0 = 6$).

609 **Histology and microscopy**

610 To verify the expression of the virus and placements of the optical fibers, mice were
611 deeply anesthetized and immediately perfused utilizing 0.1M phosphate-buffered saline
612 (PBS), followed by 4% paraformaldehyde (PFA) in PBS. The brain tissues were removed
613 and post-fixed overnight in 4% PFA. Subsequently, the brains were transferred to a 30%
614 sucrose solution at 4 °C for 48 hr. Brain samples were embedded with OCT compound
615 (NEG-50, Thermo Scientific) and cut into 50-μm sections utilizing a cryostat (HM525 NX,
616 Thermo Scientific). Brain sections were stored at -20 °C before further processing. For
617 histology examination, brain sections were washed in PBS and coverslipped with mounting
618 media containing DAPI (# F6057, Sigma). The fluorescence images were captured utilizing
619 an epifluorescence microscope (VS120, Olympus).

620 **Free-moving behavioral tests with simultaneous fiber photometry**

621 To verify the predicted behavior-related cerebral patterns, the neuronal activity of
622 primary motor area (MOP), entorhinal area (ENT) and anterior cingulate area (ACA) were
623 recorded using calcium fiber photometry during spontaneous behavior in the same arena
624 as above. AAV2/9-hSyn-GCaMP6s-WPRE-hGH pA (titer: $2.69\times10^{12}$ v .g. /mL; BrainVTA)
625 was injected into unilateral MOP (AP +0.98 mm, ML +1.5 mm, DV -0.54 mm from dura),
626 ENT (AP -3.88 mm, ML +3.75 mm, DV -2.3 mm from dura) and ACA (AP +0.14 mm, ML -
627 0.3 mm, DV -1.07 mm from dura). Three optic fibers (200 μm in diameter; NA 0.48;
628 Newdoon Co., China) were inserted into the three regions respectively, and secured with
629 the light curing flowable dental resin. Finally, the exposed skull was covered with dental
630 cement.

631 Four weeks after the surgery, the same free-moving behavioral test as above was
632 performed with simultaneous fiber photometry recording and behavioral monitoring (Fig.
633 7E). Three patch cables were connected to the three fiber implants with sleeves. Three
634 465 nm LEDs (CLED_465, Doric Lens) were used as excitation sources. Excitation power
635 at the tip of the fiber was ~20 μW. Three fluorescence optical mini cubes (FMC5_E1(465-
636 480)_F1(500-540), Doric Lens) and three visible femtowatt photoreceivers
637 (NPM_2151_FOA_FC, Doric Lens) were used for the fluorescence detection. During

recording, a software-controlled lock-in detection algorithm was implemented in the TDT RZ2 system utilizing the fiber photometry 'Gizmo' of the Synapse software (https://www.tdt.com/). The photometry signals were recorded at a sampling rate of 1017 Hz.

To analyze the photometry data, a median filter with 10-min window length was applied to the raw GCaMP6s photometry signals to capture the infra-slow baseline drift. The median-filtered calcium signal was then regressed out from the raw photometry signals using the least-squares regression. Then, the changes of calcium signals were quantified as (F-F0)/F0, where F was fluorescence intensity at each time point and F0 was calculated by mean minus double standard deviations. The calcium time series were further down-sampled to 25 Hz for subsequent analysis using the MATLAB function *interp1()*. Finally, the neuronal firing rate was evaluated by deconvolution of the normalized calcium signals (F-F0)/F0 using the first-order auto-regressive model.

For behavioral state classification, the same criteria was applied to label the spontaneous behavioral state of each mouse (details in the section of Optogenetic free-moving behavioral test).

## Comparing imaging artifacts of PMMA and $SiO_2$ fiber optic implants

A separate cohort of wild-type mice was utilized to compare imaging artifacts induced by PMMA and $SiO_2$ fiber optic implants (200 μm in diameter; NA 0.48) inserted unilaterally into the basal forebrain. To accommodate the limited space of the cryogenic RF coil, the ceramic ferrules of $SiO_2$ fiber optic implants were trimmed. All other surgical procedures and fMRI acquisition parameters were identical to those described above. The artifact size caused by the fiber optic implant in T2 or EPI images was measured, and a two-tailed paired t-test was employed to determine statistical significance.

## Data availability

The manuscript released a cell-type specific awake mouse optogenetic fMRI, behaviors and anterograde tracing dataset on basal forebrain dataset, which is available at https://cstr.cn/33145.11.BSDC.1688548668.1676512675817205762. The Allen Mouse Brain Connectivity Atlas (https://portal.brain-map.org) was published previously as open resource.

## Code availability

Codes used in this study are available at https://github.com/TrangeTung/optogenetic_BF_fMRI.

## Acknowledgements

The authors thank Jingjing Ye (iHuman Institute, ShanghaiTech Univ.) and Garth J. Thompson (iHuman Institute, ShanghaiTech Univ.) for the help in fMRI data acquisition, Ziyue Wang for the help in mouse surgery, Mouse Animal Facility of CEBSIT for animal care, and the Brain Science Data Center, Chinese Academy of Sciences for dataset release. This work was supported by the National Science and Technology Innovation 2030 Major Program (2021ZD0200100 to ZL), Strategic Priority Research Program of Chinese Academy of Sciences (XDBS01030100 to ZL and MX), Pioneer Hundreds of Talents Program from the Chinese Academy of Sciences (to ZL), Shanghai Municipal Science and Technology Major Project (2018SHZDZX05 to ZL and MX, 2021SHZDZX to MX), the National Natural Science Foundation of China (82171899 to ZL, 32221003 to MX), Lingang Laboratory (LG202104-02-06 to ZL). CAS Project for Young Scientists in Basic Research (YSBR-071 to MX), Lingang Laboratory & National Key Laboratory of Human Factors Engineering Joint Grant (LG-TKN-202203-01 to MX), Shanghai Post-doctoral Excellence Program (2021399 to WP), Postdoctoral Innovative Talents Supporting Program (WP),

China Postdoctoral Science Foundation (W.P.), Specail Research Assistant Project of the Chinese Academy of Sciences (WP).

## Author Contributions Statement

Y.Z., C.T., M.X. and Z.L. designed the study; Y.Z., C.T., J.L., Y.X., M.P., K.Z. and W.L. collected the MRI and behavioral data; Y.Z., C.T. and Z.L. preprocessed and organized the MRI and behavioral data; W.P. and M.X. collected and preprocessed the anterograde tracing data; C.T., Y.Z. and Z.L. conducted the decoding modeling. Y.Z., C.T., M.X. and Z.L. wrote the original draft and revised the draft. All authors discussed and approved the manuscript.

## Competing Interests Statement

The authors declare no competing interests.

# References


1. Yang, C., Thankachan, S., McCarley, R.W., and Brown, R.E. (2017). The menagerie of the basal forebrain: how many (neural) species are there, what do they look like, how do they behave and who talks to whom? Current Opinion in Neurobiology *44*, 159–166. 10.1016/j.conb.2017.05.004.
2. Zaborszky, L., Csordas, A., Mosca, K., Kim, J., Gielow, M.R., Vadasz, C., and Nadasdy, Z. (2015). Neurons in the Basal Forebrain Project to the Cortex in a Complex Topographic Organization that Reflects Corticocortical Connectivity Patterns: An Experimental Study Based on Retrograde Tracing and 3D Reconstruction. Cerebral Cortex *25*, 118–137. 10.1093/cercor/bht210.
3. Xu, M., Chung, S., Zhang, S., Zhong, P., Ma, C., Chang, W.-C., Weissbourd, B., Sakai, N., Luo, L., Nishino, S., et al. (2015). Basal forebrain circuit for sleep-wake control. Nat Neurosci *18*, 1641–1647. 10.1038/nn.4143.
4. Do, J.P., Xu, M., Lee, S.-H., Chang, W.-C., Zhang, S., Chung, S., Yung, T.J., Fan, J.L., Miyamichi, K., Luo, L., et al. (2016). Cell type-specific long-range connections of basal forebrain circuit. eLife *5*, e13214. 10.7554/eLife.13214.
5. Ballinger, E.C., Ananth, M., Talmage, D.A., and Role, L.W. (2016). Basal Forebrain Cholinergic Circuits and Signaling in Cognition and Cognitive Decline. Neuron *91*, 1199–1218. 10.1016/j.neuron.2016.09.006.
6. Geula, C., Dunlop, S.R., Ayala, I., Kawles, A.S., Flanagan, M.E., Gefen, T., and Mesulam, M. (2021). Basal forebrain cholinergic system in the dementias: Vulnerability, resilience, and resistance. J. Neurochem. *158*, 1394–1411. 10.1111/jnc.15471.
7. Giacobini, E., Cuello, A.C., and Fisher, A. (2022). Reimagining cholinergic therapy for Alzheimer's disease. Brain *145*, 2250–2275. 10.1093/brain/awac096.
8. Chaves-Coira, I., García-Magro, N., Zegarra-Valdivia, J., Torres-Alemán, I., and Núñez, Á. (2023). Cognitive Deficits in Aging Related to Changes in Basal Forebrain Neuronal Activity. Cells *12*, 1477. 10.3390/cells12111477.
9. Ananth, M.R., Rajebhosale, P., Kim, R., Talmage, D.A., and Role, L.W. (2023). Basal forebrain cholinergic signalling: development, connectivity and roles in cognition. Nat Rev Neurosci. 10.1038/s41583-023-00677-x.
10. Grossberg, S. (2017). Acetylcholine Neuromodulation in Normal and Abnormal Learning and Memory: Vigilance Control in Waking, Sleep, Autism, Amnesia and Alzheimer's Disease. Front. Neural Circuits *11*, 82. 10.3389/fncir.2017.00082.
11. Luchicchi, A., Bloem, B., ViaÃ±a, J.N.M., Mansvelder, H.D., and Role, L.W. (2014). Illuminating the role of cholinergic signaling in circuits of attention and emotionally salient behaviors. Front. Synaptic Neurosci. *6*. 10.3389/fnsyn.2014.00024.

12. Okada, K., Hashimoto, K., and Kobayashi, K. (2022). Cholinergic regulation of object recognition memory. Front. Behav. Neurosci. *16*, 996089. 10.3389/fnbeh.2022.996089.

13. Harrison, T.C., Pinto, L., Brock, J.R., and Dan, Y. (2016). Calcium Imaging of Basal Forebrain Activity during Innate and Learned Behaviors. Front. Neural Circuits *10*. 10.3389/fncir.2016.00036.

14. Peng, W., Wu, Z., Song, K., Zhang, S., Li, Y., and Xu, M. (2020). Regulation of sleep homeostasis mediator adenosine by basal forebrain glutamatergic neurons. Science *369*, eabb0556. 10.1126/science.abb0556.

15. McKenna, J.T., Yang, C., Bellio, T., Anderson-Chernishof, M.B., Gamble, M.C., Hulverson, A., McCoy, J.G., Winston, S., Hodges, E., Katsuki, F., et al. (2021). Characterization of basal forebrain glutamate neurons suggests a role in control of arousal and avoidance behavior. Brain Struct Funct *226*, 1755–1778. 10.1007/s00429-021-02288-7.

16. Swanson, J.L., Ortiz-Guzman, J., Srivastava, S., Chin, P.-S., Dooling, S.W., Hanson Moss, E., Kochukov, M.Y., Hunt, P.J., Patel, J.M., Pekarek, B.T., et al. (2022). Activation of basal forebrain-to-lateral habenula circuitry drives reflexive aversion and suppresses feeding behavior. Sci Rep *12*, 22044. 10.1038/s41598-022-26306-8.

17. Avila, I., and Lin, S.-C. (2014). Distinct neuronal populations in the basal forebrain encode motivational salience and movement. Front. Behav. Neurosci. *8*. 10.3389/fnbeh.2014.00421.

18. Liu, X., de Zwart, J.A., Schölvinck, M.L., Chang, C., Ye, F.Q., Leopold, D.A., and Duyn, J.H. (2018). Subcortical evidence for a contribution of arousal to fMRI studies of brain activity. Nat Commun *9*, 395. 10.1038/s41467-017-02815-3.

19. Turchi, J., Chang, C., Ye, F.Q., Russ, B.E., Yu, D.K., Cortes, C.R., Monosov, I.E., Duyn, J.H., and Leopold, D.A. (2018). The Basal Forebrain Regulates Global Resting-State fMRI Fluctuations. Neuron *97*, 940-952.e4. 10.1016/j.neuron.2018.01.032.

20. Shah, D., Blockx, I., Keliris, G.A., Kara, F., Jonckers, E., Verhoye, M., and Van der Linden, A. (2016). Cholinergic and serotonergic modulations differentially affect large-scale functional networks in the mouse brain. Brain Struct Funct *221*, 3067–3079. 10.1007/s00429-015-1087-7.

21. Shah, D., Blockx, I., Guns, P.-J., De Deyn, P.P., Van Dam, D., Jonckers, E., Delgado y Palacios, R., Verhoye, M., and Van der Linden, A. (2015). Acute modulation of the cholinergic system in the mouse brain detected by pharmacological resting-state functional MRI. NeuroImage *109*, 151–159. 10.1016/j.neuroimage.2015.01.009.

22. Peeters, L.M., van den Berg, M., Hinz, R., Majumdar, G., Pintelon, I., and Keliris, G.A. (2020). Cholinergic Modulation of the Default Mode Like Network in Rats. iScience *23*, 101455. 10.1016/j.isci.2020.101455.

23. Nair, J., Klaassen, A.-L., Poirot, J., Vyssotski, A., Rasch, B., and Rainer, G. (2016). Gamma band directional interactions between basal forebrain and visual cortex during wake and sleep states. Journal of Physiology-Paris *110*, 19–28. 10.1016/j.jphysparis.2016.11.011.

24. Nair, J., Klaassen, A.-L., Arato, J., Vyssotski, A.L., Harvey, M., and Rainer, G. (2018). Basal forebrain contributes to default mode network regulation. Proc. Natl. Acad. Sci. U.S.A. *115*, 1352–1357. 10.1073/pnas.1712431115.

25. Lozano-Montes, L., Dimanico, M., Mazloum, R., Li, W., Nair, J., Kintscher, M., Schneggenburger, R., Harvey, M., and Rainer, G. (2020). Optogenetic Stimulation of Basal Forebrain Parvalbumin Neurons Activates the Default Mode Network and Associated Behaviors. Cell Reports *33*, 108359. 10.1016/j.celrep.2020.108359.

26. Chen, X., Tong, C., Han, Z., Zhang, K., Bo, B., Feng, Y., and Liang, Z. (2020). Sensory evoked fMRI paradigms in awake mice. NeuroImage *204*, 116242. 10.1016/j.neuroimage.2019.116242.

27. Han, Z., Chen, W., Chen, X., Zhang, K., Tong, C., Zhang, X., Li, C.T., and Liang, Z. (2019). Awake and behaving mouse fMRI during Go/No-Go task. NeuroImage *188*, 733–742. 10.1016/j.neuroimage.2019.01.002.

28. Xu, W., Pei, M., Zhang, K., Tong, C., Bo, B., Feng, J., Zhang, X.-Y., and Liang, Z. (2022). A systematically optimized awake mouse fMRI paradigm. https://www.biorxiv.org/content/10.1101/2022.11.16.516376v1.full.

29. Yu, Y., Qiu, Y., Li, G., Zhang, K., Bo, B., Pei, M., Ye, J., Thompson, G.J., Cang, J., Fang, F., et al. (2023). Sleep fMRI with simultaneous electrophysiology at 9.4 T in male mice. Nat Commun *14*, 1651. 10.1038/s41467-023-37352-9.

30. Coletta, L., Pagani, M., Whitesell, J.D., Harris, J.A., Bernhardt, B., and Gozzi, A. (2020). Network structure of the mouse brain connectome with voxel resolution. Sci. Adv. *6*, eabb7187. 10.1126/sciadv.abb7187.

31. Knox, J.E., Harris, K.D., Graddis, N., Whitesell, J.D., Zeng, H., Harris, J.A., Shea-Brown, E., and Mihalas, S. (2019). High-resolution data-driven model of the mouse connectome. Network Neuroscience *3*, 217–236. 10.1162/netn_a_00066.

32. Espinosa, N., Alonso, A., Morales, C., Espinosa, P., Chávez, A.E., and Fuentealba, P. (2019). Basal Forebrain Gating by Somatostatin Neurons Drives Prefrontal Cortical Activity. Cerebral Cortex *29*, 42–53. 10.1093/cercor/bhx302.

33. Klaassen, A.-L., Heiniger, A., Vaca Sánchez, P., Harvey, M.A., and Rainer, G. (2021). Ventral pallidum regulates the default mode network, controlling transitions between internally and externally guided behavior. Proceedings of the National Academy of Sciences *118*, e2103642118. 10.1073/pnas.2103642118.

34. Raichle, M.E., MacLeod, A.M., Snyder, A.Z., Powers, W.J., Gusnard, D.A., and Shulman, G.L. (2001). A default mode of brain function. Proc. Natl. Acad. Sci. U.S.A. *98*, 676–682. 10.1073/pnas.98.2.676.

35. Harrison, B.J., Davey, C.G., Savage, H.S., Jamieson, A.J., Leonards, C.A., Moffat, B.A., Glarin, R.K., and Steward, T. (2022). Dynamic subcortical modulators of human default mode network function. Cereb Cortex *32*, 4345–4355. 10.1093/cercor/bhab487.

36. Harrison, B.J., Pujol, J., López-Solà, M., Hernández-Ribas, R., Deus, J., Ortiz, H., Soriano-Mas, C., Yücel, M., Pantelis, C., and Cardoner, N. (2008). Consistency and functional specialization in the default mode brain network. Proc Natl Acad Sci U S A *105*, 9781–9786. 10.1073/pnas.0711791105.

37. Miller, K.J., Weaver, K.E., and Ojemann, J.G. (2009). Direct electrophysiological measurement of human default network areas. Proceedings of the National Academy of Sciences *106*, 12174–12177. 10.1073/pnas.0902071106.

38. Giovannini, M.G., Rakovska, A., Benton, R.S., Pazzagli, M., Bianchi, L., and Pepeu, G. (2001). Effects of novelty and habituation on acetylcholine, GABA, and glutamate release from the frontal cortex and hippocampus of freely moving rats. Neuroscience *106*, 43–53. 10.1016/S0306-4522(01)00266-4.

39. Meeter, M., Murre, J. m. j., and Talamini, L. m. (2004). Mode shifting between storage and recall based on novelty detection in oscillating hippocampal circuits. Hippocampus *14*, 722–741. 10.1002/hipo.10214.

40. Esaki, H., Izumi, S., Fukao, A., Ito, S., Nishitani, N., Deyama, S., and Kaneda, K. (2021). Nicotine Enhances Object Recognition Memory *via* Stimulating α4β2 and α7 Nicotinic Acetylcholine Receptors in the Medial Prefrontal Cortex of Mice. Biological & Pharmaceutical Bulletin *44*, 1007–1013. 10.1248/bpb.b21-00314.

41. Leiras, R., Cregg, J.M., and Kiehn, O. (2022). Brainstem Circuits for Locomotion. Annu Rev Neurosci *45*, 63–85. 10.1146/annurev-neuro-082321-025137.

42. Grandjean, J., Corcoba, A., Kahn, M.C., Upton, A.L., Deneris, E.S., Seifritz, E., Helmchen, F., Mansuy, I.M., Mann, E.O., Rudin, M., et al. (2019). A brain-wide functional map of the serotonergic responses toacute stress and fluoxetine. Nat Commun *10*, 350. 10.1038/s41467-018-08256-w.

43. Jung, W.B., Jiang, H., Lee, S., and Kim, S.-G. (2022). Dissection of brain-wide resting-state and functional somatosensory circuits by fMRI with optogenetic silencing. Proc. Natl. Acad. Sci. U.S.A. *119*, e2113313119. 10.1073/pnas.2113313119.

44. Moon, H.S., Jiang, H., Vo, T.T., Jung, W.B., Vazquez, A.L., and Kim, S.-G. (2021). Contribution of Excitatory and Inhibitory Neuronal Activity to BOLD fMRI. Cerebral Cortex *31*, 4053–4067. 10.1093/cercor/bhab068.

45. Shim, H.-J., Im, G.H., Jung, W.B., Moon, H.S., Dinh, T.N.A., Lee, J.-Y., and Kim, S.-G. (2022). Protocol for mouse optogenetic fMRI at ultrahigh magnetic fields. STAR Protocols *3*, 101846. 10.1016/j.xpro.2022.101846.

46. Lohani, S., Poplawsky, A.J., Kim, S.-G., and Moghaddam, B. (2017). Unexpected global impact of VTA dopamine neuron activation as measured by opto-fMRI. Mol Psychiatry *22*, 585–594. 10.1038/mp.2016.102.

47. Liang, Z., Watson, G.D.R., Alloway, K.D., Lee, G., Neuberger, T., and Zhang, N. (2015). Mapping the functional network of medial prefrontal cortex by combining optogenetics and fMRI in awake rats. NeuroImage *117*, 114–123. 10.1016/j.neuroimage.2015.05.036.

48. Chan, R.W., Cron, G.O., Asaad, M., Edelman, B.J., Lee, H.J., Adesnik, H., Feinberg, D., and Lee, J.H. (2022). Distinct local and brain-wide networks are activated by optogenetic stimulation of neurons specific to each layer of motor cortex. NeuroImage *263*, 119640. 10.1016/j.neuroimage.2022.119640.

49. Yu, X., He, Y., Wang, M., Merkle, H., Dodd, S.J., Silva, A.C., and Koretsky, A.P. (2016). Sensory and optogenetically driven single-vessel fMRI. Nat Methods *13*, 337–340. 10.1038/nmeth.3765.

50. Desai, M., Kahn, I., Knoblich, U., Bernstein, J., Atallah, H., Yang, A., Kopell, N., Buckner, R.L., Graybiel, A.M., Moore, C.I., et al. (2011). Mapping brain networks in awake mice using combined optical neural control and fMRI. Journal of Neurophysiology *105*, 1393–1405. 10.1152/jn.00828.2010.

51. Ferenczi, E.A., Zalocusky, K.A., Liston, C., Grosenick, L., Warden, M.R., Amatya, D., Katovich, K., Mehta, H., Patenaude, B., Ramakrishnan, C., et al. (2016). Prefrontal cortical regulation of brainwide circuit dynamics and reward-related behavior. Science *351*, aac9698. 10.1126/science.aac9698.

52. Cover, C.G., Kesner, A.J., Ukani, S., Stein, E.A., Ikemoto, S., Yang, Y., and Lu, H. (2021). Whole brain dynamics during optogenetic self-stimulation of the medial prefrontal cortex in mice. Commun Biol *4*, 66. 10.1038/s42003-020-01612-x.

53. Paasonen, J., Stenroos, P., Salo, R.A., Kiviniemi, V., and Gröhn, O. (2018). Functional connectivity under six anesthesia protocols and the awake condition in rat brain. NeuroImage *172*, 9–20. 10.1016/j.neuroimage.2018.01.014.

54. Reimann, H.M., and Niendorf, T. (2020). The (Un)Conscious Mouse as a Model for Human Brain Functions: Key Principles of Anesthesia and Their Impact on Translational Neuroimaging. Front. Syst. Neurosci. *14*, 8. 10.3389/fnsys.2020.00008.

55. Wapler, M.C., Leupold, J., Dragonu, I., von Elverfeld, D., Zaitsev, M., and Wallrabe, U. (2014). Magnetic properties of materials for MR engineering, micro-MR and beyond. Journal of Magnetic Resonance *242*, 233–242. 10.1016/j.jmr.2014.02.005.

56. Esaki, H., Izumi, S., Fukao, A., Nishitani, N., Deyama, S., and Kaneda, K. (2021). Nicotine enhances object recognition memory through inhibition of voltage-dependent potassium 7 channels in the medial prefrontal cortex of mice. Journal of Pharmacological Sciences *147*, 58–61. 10.1016/j.jphs.2021.05.009.

57. Hanson, E., Brandel-Ankrapp, K.L., and Arenkiel, B.R. (2021). Dynamic Cholinergic Tone in the Basal Forebrain Reflects Reward-Seeking and Reinforcement During Olfactory Behavior. Front Cell Neurosci *15*, 635837. 10.3389/fncel.2021.635837.

58. Pinto, L., Goard, M.J., Estandian, D., Xu, M., Kwan, A.C., Lee, S.-H., Harrison, T.C., Feng, G., and Dan, Y. (2013). Fast modulation of visual perception by basal forebrain cholinergic neurons. Nat Neurosci *16*, 1857–1863. 10.1038/nn.3552.

59. Nelson, A., and Mooney, R. (2016). The Basal Forebrain and Motor Cortex Provide Convergent yet Distinct Movement-Related Inputs to the Auditory Cortex. Neuron *90*, 635–648. 10.1016/j.neuron.2016.03.031.

60. Stafford, J.M., Jarrett, B.R., Miranda-Dominguez, O., Mills, B.D., Cain, N., Mihalas, S., Lahvis, G.P., Lattal, K.M., Mitchell, S.H., David, S.V., et al. (2014). Large-scale topology and the default mode network in the mouse connectome. Proc Natl Acad Sci U S A *111*, 18745–18750. 10.1073/pnas.1404346111.

61. Alves, P.N., Foulon, C., Karolis, V., Bzdok, D., Margulies, D.S., Volle, E., and Thiebaut de Schotten, M. (2019). An improved neuroanatomical model of the default-mode network reconciles previous neuroimaging and neuropathological findings. Commun Biol *2*, 370. 10.1038/s42003-019-0611-3.

62. Li, J., Curley, W.H., Guerin, B., Dougherty, D.D., Dalca, A.V., Fischl, B., Horn, A., and Edlow, B.L. (2021). Mapping the subcortical connectivity of the human default mode network. NeuroImage *245*, 118758. 10.1016/j.neuroimage.2021.118758.

63. Tong, C., Liu, C., Zhang, K., Bo, B., Xia, Y., Yang, H., Feng, Y., and Liang, Z. (2022). Multimodal analysis demonstrating the shaping of functional gradients in the marmoset brain. Nat Commun *13*, 6584. 10.1038/s41467-022-34371-w.

64. Shine, J.M., Breakspear, M., Bell, P.T., Ehgoetz Martens, K.A., Shine, R., Koyejo, O., Sporns, O., and Poldrack, R.A. (2019). Human cognition involves the dynamic integration of neural activity and neuromodulatory systems. Nat Neurosci *22*, 289–296. 10.1038/s41593-018-0312-0.

65. Chang, C., Leopold, D.A., Schölvinck, M.L., Mandelkow, H., Picchioni, D., Liu, X., Ye, F.Q., Turchi, J.N., and Duyn, J.H. (2016). Tracking brain arousal fluctuations with fMRI. Proc. Natl. Acad. Sci. U.S.A. *113*, 4518–4523. 10.1073/pnas.1520613113.

66. Fox, M.D., Snyder, A.Z., Vincent, J.L., Corbetta, M., Van Essen, D.C., and Raichle, M.E. (2005). The human brain is intrinsically organized into dynamic, anticorrelated functional networks. Proceedings of the National Academy of Sciences *102*, 9673–9678. 10.1073/pnas.0504136102.

67. Shulman, G.L., Corbetta, M., Buckner, R.L., Fiez, J.A., Miezin, F.M., Raichle, M.E., and Petersen, S.E. (1997). Common Blood Flow Changes across Visual Tasks: I. Increases in Subcortical Structures and Cerebellum but Not in Nonvisual Cortex. J Cogn Neurosci *9*, 624–647. 10.1162/jocn.1997.9.5.624.

68. Jung, W.B., Im, G.H., Jiang, H., and Kim, S.-G. (2021). Early fMRI responses to somatosensory and optogenetic stimulation reflect neural information flow. Proc. Natl. Acad. Sci. U.S.A. *118*, e2023265118. 10.1073/pnas.2023265118.

69. Zerbi, V., Grandjean, J., Rudin, M., and Wenderoth, N. (2015). Mapping the mouse brain with rs-fMRI: An optimized pipeline for functional network identification. NeuroImage *123*, 11–21. 10.1016/j.neuroimage.2015.07.090.

70. Beckmann, C.F., and Smith, S.M. (2004). Probabilistic independent component analysis for functional magnetic resonance imaging. IEEE Transactions on Medical Imaging *23*, 137–152. 10.1109/TMI.2003.822821.

71. Grandjean, J., Zerbi, V., Balsters, J.H., Wenderoth, N., and Rudin, M. (2017). Structural Basis of Large-Scale Functional Connectivity in the Mouse. J Neurosci *37*, 8092–8101. 10.1523/JNEUROSCI.0438-17.2017.

72. Oh, S.W., Harris, J.A., Ng, L., Winslow, B., Cain, N., Mihalas, S., Wang, Q., Lau, C., Kuan, L., Henry, A.M., et al. (2014). A mesoscale connectome of the mouse brain. Nature *508*, 207–214. 10.1038/nature13186.

# Figures and Figure Legends

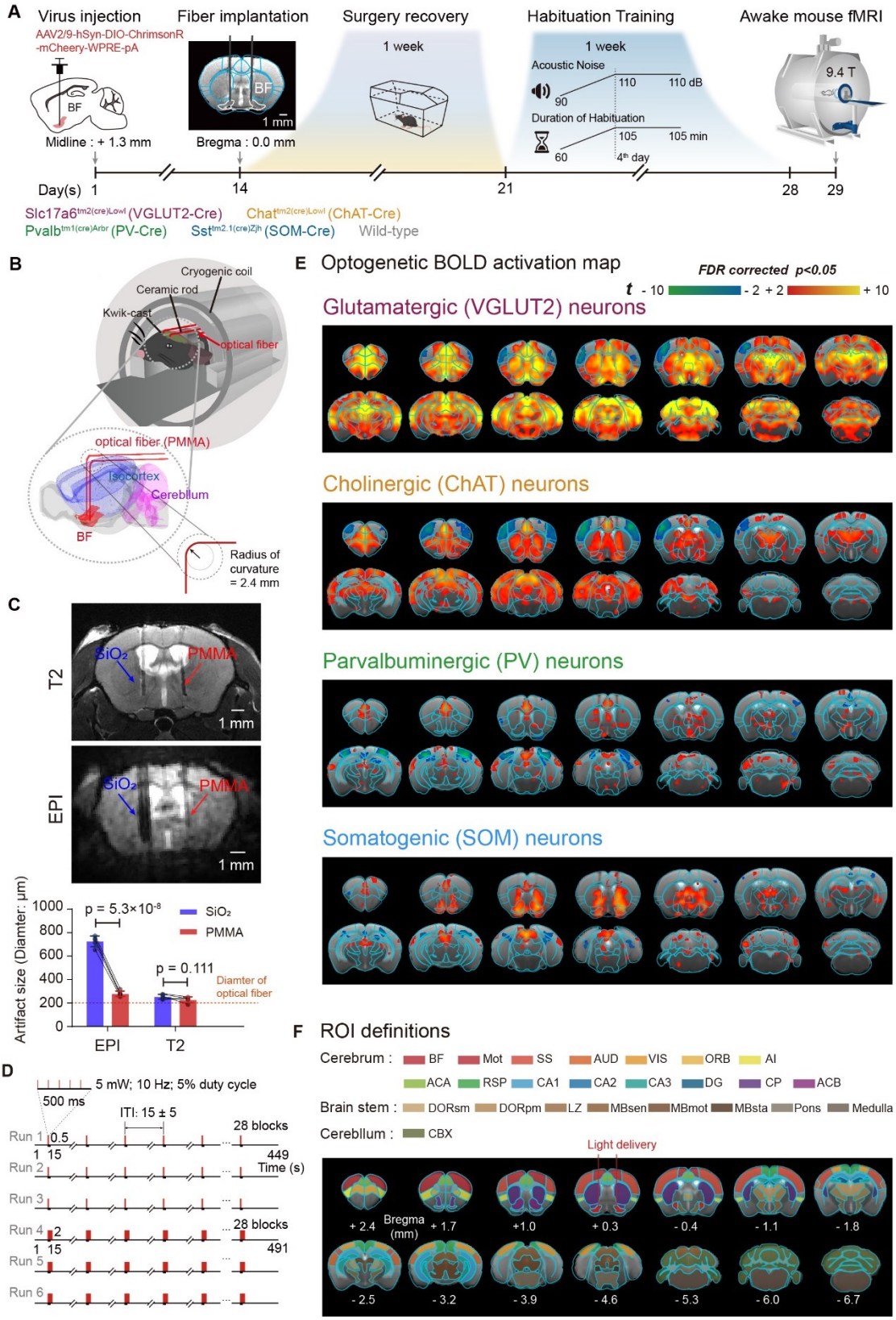

952 **Figure 1 | Whole brain opto-fMRI responses driven by cell-type specific neuronal**
953 **activations of the basal forebrain in awake mice.**
954 (A) Schematic setup of opto-fMRI and experimental timeline.
955 (B) Flexible PMMA fiber for optogenetic light delivery within cryogenic coil. Light was
956 delivered to bilateral basal forebrain (BF) via two PMMA optical fibers. PMMA,
957 polymethylmethacrylate.
958 (C) Reduced image artifact by PMMA optical fiber compared to SiO2 fiber. SiO2, silicon
959 dioxide. Statistical significance was determined using paired t-test (two tails, N=5 animals).
960 Error bar, the standard error of the mean.
961 (D) Optogenetic stimulation paradigm.
962 (E) BOLD responses under optogenetic stimulations of cell-type specific BF neurons with
963 FDR corrected $p < 0.05$.
964 (F) Region-of-interest (ROI) definitions based on CCFv3 Allen mouse brain atlas.
965 Abbreviations were list in Supplementary Table 1.
966

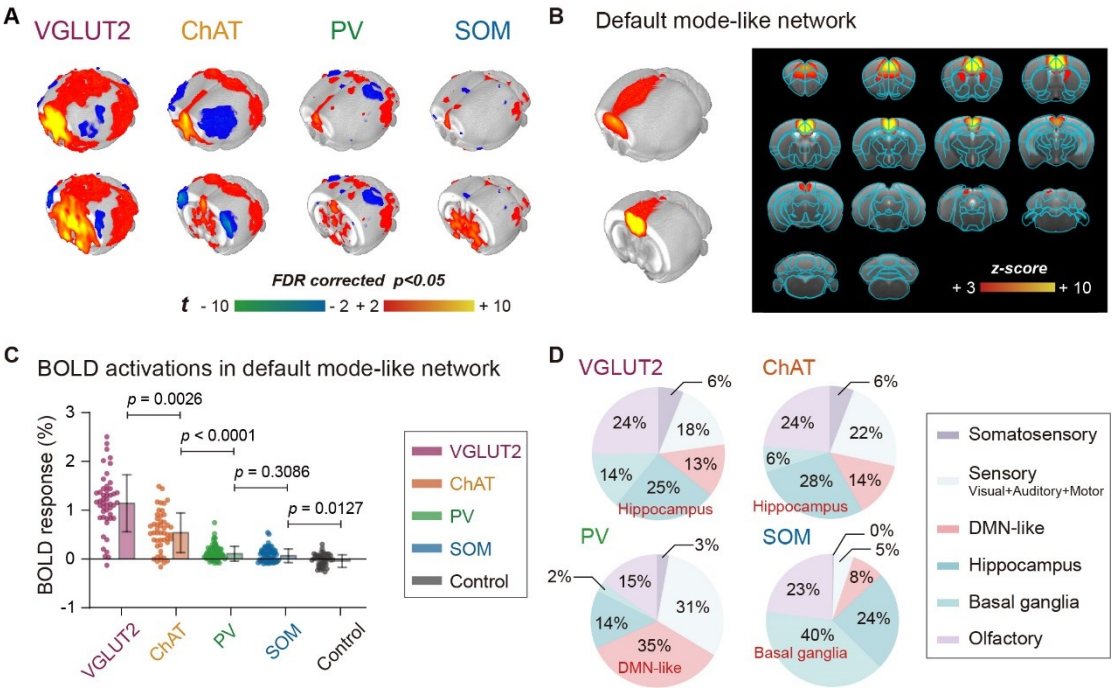


**Figure 2 | Consistent activations in mouse default mode-like network (DMN-like) under cell-type specific optogenetic stimulations of basal forebrain neurons.**

(A) BOLD activation maps in 3D view under cell-type specific optogenetic stimulations of basal forebrain (BF) neurons. The activation maps were same as Fig. 1E.

(B) DMN-like component of mouse in 3D view (left panel) and axial slice view (right panel).

(C) Significant BOLD activations in DMN-like regions under cell-type specific manipulation on BF neurons. Statistical significance was determined using a one-way ANOVA followed by Tukey's post hoc test for group comparison. Each dot represented an individual EPI run. Error bar, the standard deviation (S.D.) of the mean.

(D) Highest specificity of DMN-like activations modulated by BF PV neurons. Pie charts showing the composition by mouse functional networks for the cell-type specific opto-fMRI responses.

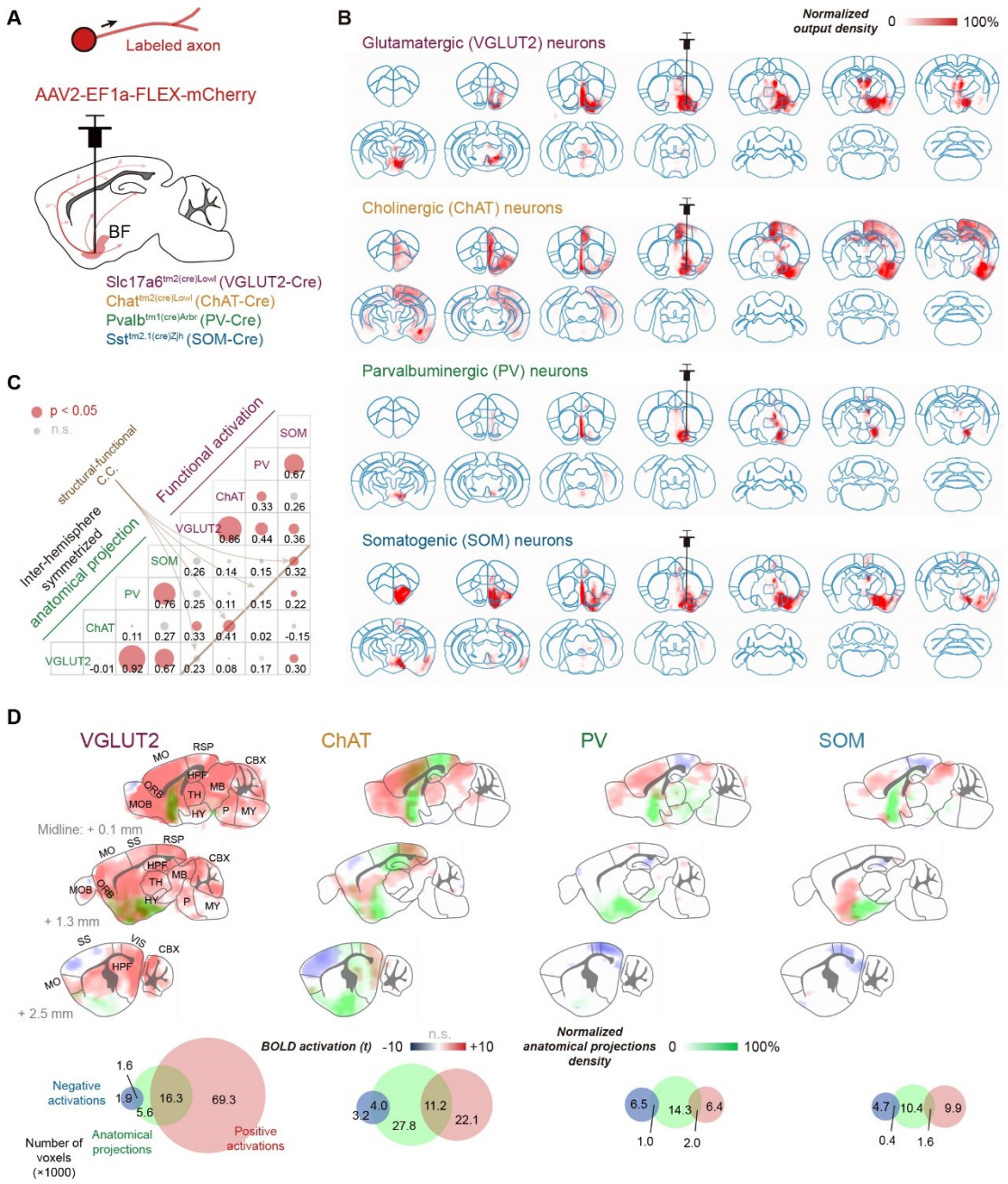


**Figure 3 | Direct anatomical projections weakly contribute to opto-fMRI activation patterns of BF neurons.**

(A) Viral injection procedure for tracing BF projections.

(B) Whole-brain anatomical projections from 4 BF neuron types.

(C) Weak spatial similarities (brown line) between anatomical projection and functional activation maps for four BF neuron types. The size of each circle indicates the spatial similarity (Pearson's correlation coefficients, C.C.).

(D) Spatial maps (upper panel) and quantitative evaluations (lower panel) of the overlay between anatomical projections and functional activations.

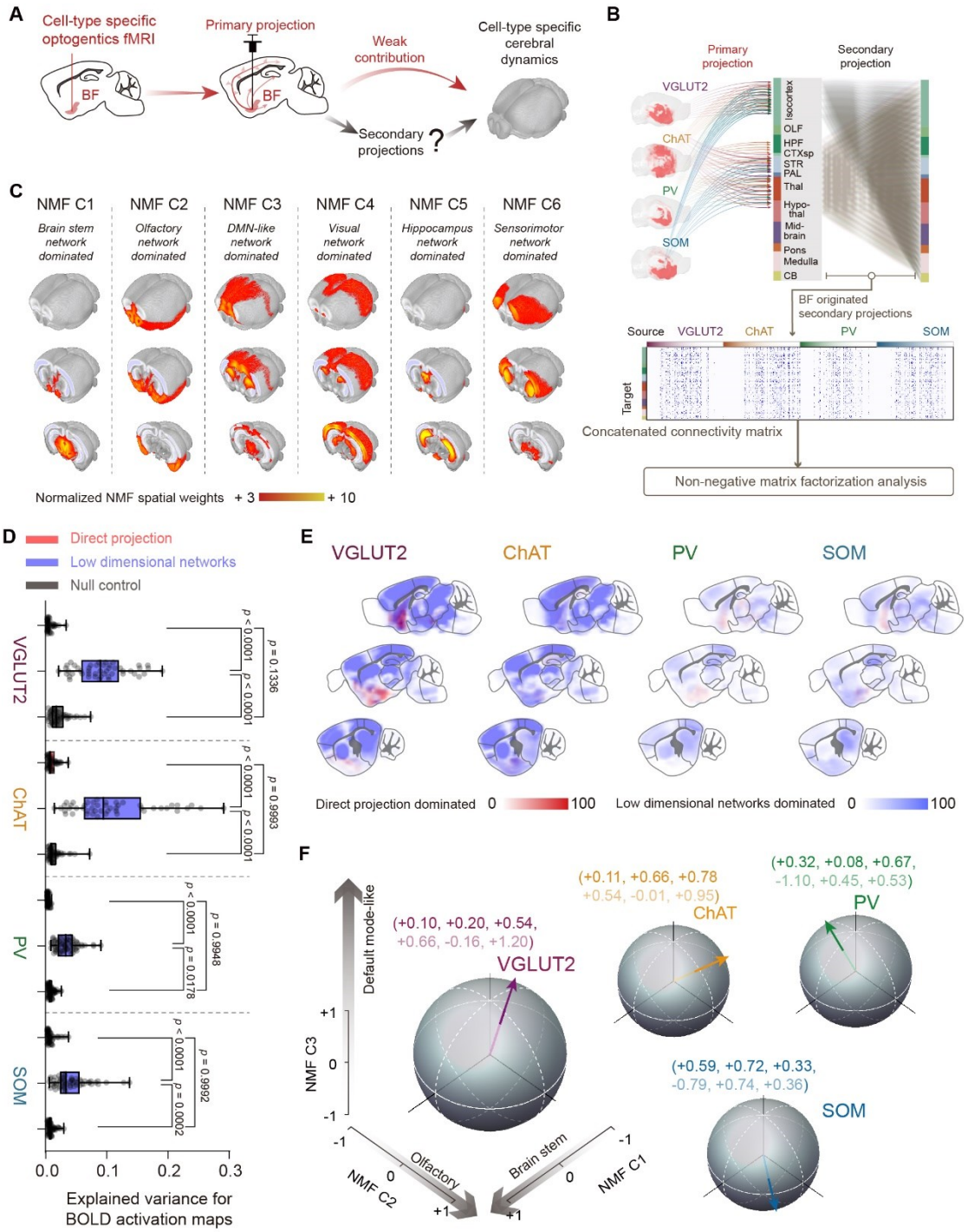


**Figure 4 | BF originated low dimensional structural networks significantly contributed to cell-type specific opto-fMRI activations.**

(A) Hypothesis of the contribution of secondary projections on cell-type specific opto-fMRI activations.

(B) Computational pipeline of non-negative matrix factorization (NMF) on BF originated whole-brain mesoscopic secondary projections.

(C) Spatial maps of three low dimensional structural networks (i.e., the first six NMF components) in 3D view.

(D-E) Quantification (D) and spatial distributions (E) of explained variance for opto-fMRI activations from the direct projections and low dimensional structural networks (as in Figure 4C) respectively. Statistical significance was calculated by two-tailed paired t-test. Notably, the null control was constructed by spatially shuffling the BOLD activation maps. Each dot represented an individual EPI run. Box, 25-75% range and median line; whisker, minimum to maximum range; plus mark, the mean value.

(F) Cell-type specific opto-fMRI activations in six dimensional NMF space. Feature vector for each BF cell type was normalized by its magnitude.

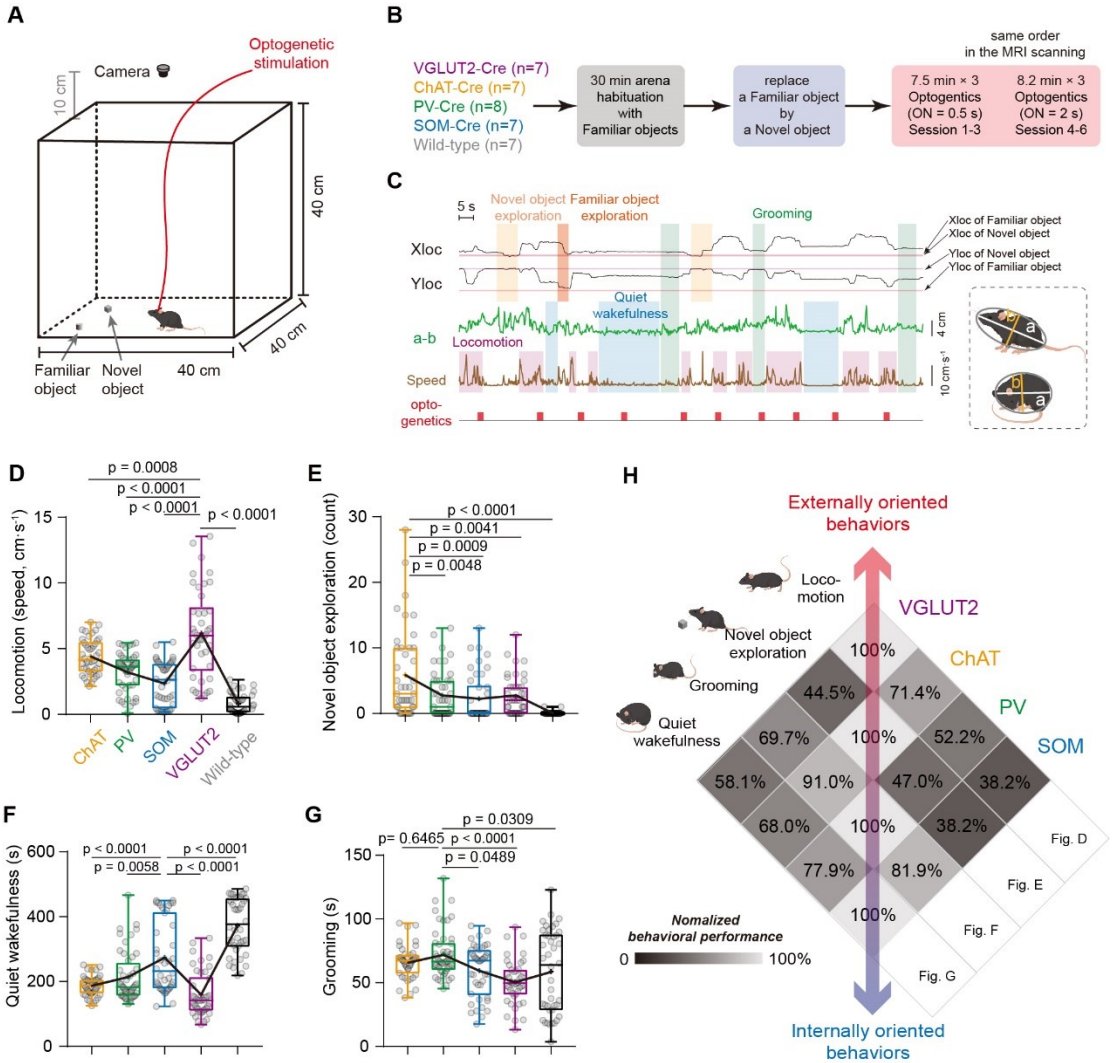


**Figure 5 | Inhibitory (PV and SOM) or excitatory (VGLUT2 and ChAT) neurons in BF supported internally or externally oriented behaviors respectively.**

(A-B) Schematic of the free-moving behavioral experiments under optogenetic stimulations.

(C) Representative behavioral traces.

(D-G) Behavior performances under optogenetic activations of four BF neuron types, including locomotion (D), novel object exploration (E), quiet wakefulness (F) and grooming (G). Details of multiple comparison across cell-types were list in supplementary Table 2. Each dot represented the averaged behavioral performance in each experimental session. Box, 25-75% range and median line; whisker, minimum to maximum range; plus mark, the mean value.

(H) Ranking of preferred optogenetic stimulated BF cell types across mouse behaviors showed inhibitory or excitatory neurons in BF supported internally or externally oriented behaviors respectively. The behavioral performance was normalized by dividing its maximum for the mean of each behavior (D-G).

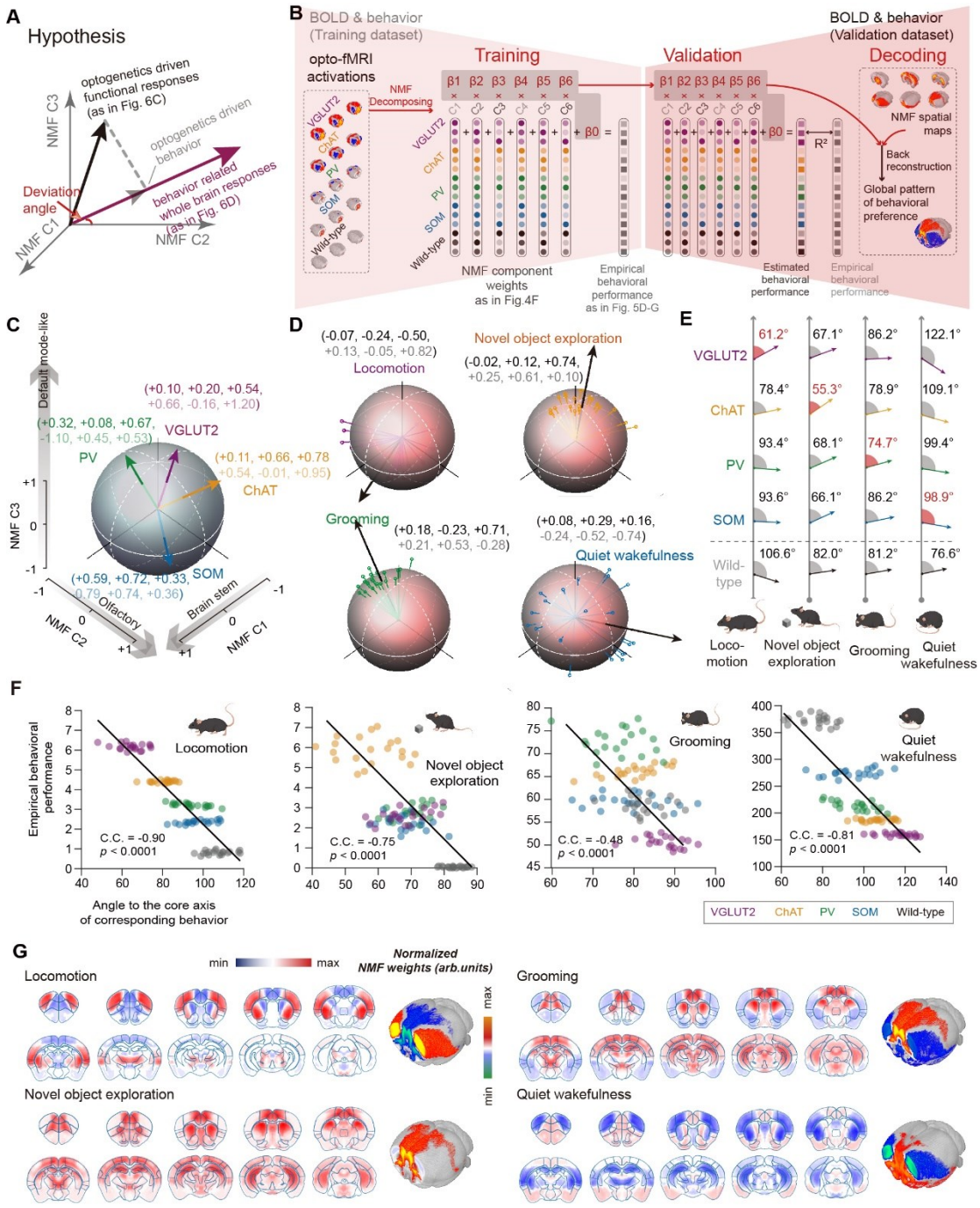


**Figure 6 | A decoding model predicted the global patterns of opto-induced behaviors outside the magnet based on the low dimensional networks.**

(A) Hypothesis: cell-type specific activation maps and behavior-related cerebral patterns shared common low-dimensional (NMF) space as the same optogenetic stimulation paradigm was applied in opto-fMRI and behavioral test.

(B)Schematics of decoding model to link BF modulated BOLD activations and behavioral preference.

(C-D) Feature vectors of cell-type specific BF modulations (C, as in Fig. 3G) and predicted behavior-related cerebral patterns (D). Colored lines and black arrows, predicted and corresponding averaged feature vectors for each behavior. Each colored line represented

an individual decoding process (N = 20). We randomly chosen 3 sessions as training dataset out of 6 sessions for each process and repeated this process to cover all combinations.

(E) Deviation angles between feature vectors in Fig. C and Fig. D. Red shadow represented the minimal angle across cell-type specific BF modulations in each behavior (wild-type excluded), indicated the most distinct behavioral preference.

(F) Significant correlations between deviation angles and empirical behavioral performance. Smaller deviation angles indicated shorter distances to the behavioral feature vectors in NMF space, i.e., higher behavioral preference of BF cell types. Each dot represented an individual decoding process (N = 20, as in Figure 5D-G). Black line represented the best linear fit. C.C., Pearson's correlation coefficients.

(G) Predicted cerebral responses of mouse behaviors based on the low dimensional NMF space.

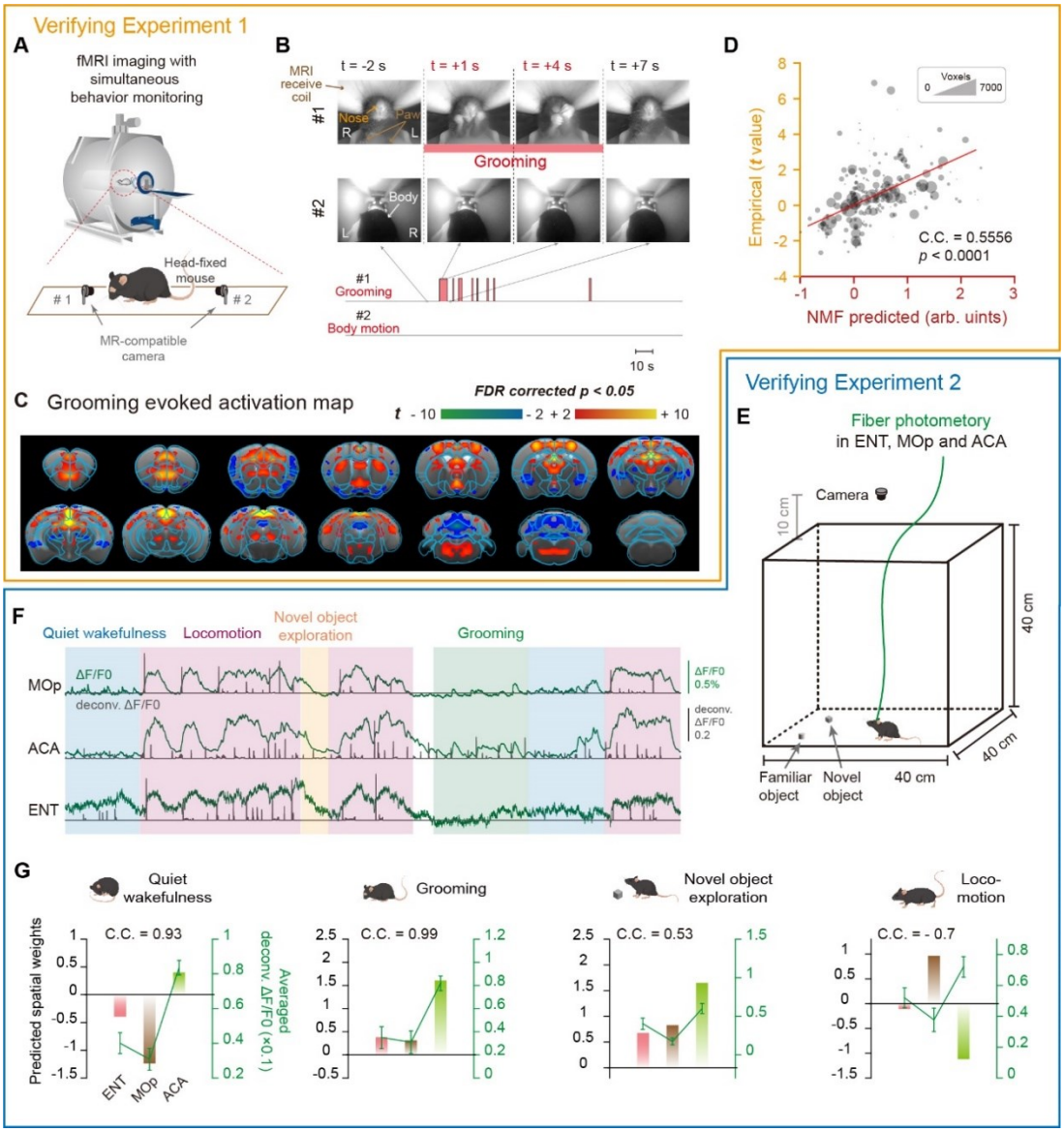


**Figure 7 | Experimental validations of predicted behavior-related cerebral responses.**
(A) Schematic of the fMRI experimental setup with simultaneous behavior monitoring.
(B) Example of spontaneous grooming during awake mouse fMRI scanning.
(C) Empirical activation maps of mouse spontaneous grooming.
(D) Significant correlation between empirical and predicted activation maps of mouse grooming. Each dot represented an individual brain region, scaled according to the voxel number of each region. C.C., Pearson's correlation coefficients.
(E) Schematic of the free-moving behavioral experiments with simultaneous calcium fiber photometry in primary motor area (MOp), anterior cingulate area (ACA) and entorhinal cortex (ENT) respectively.
(F) Representative calcium signals in MOp, ACA and ENT regions during spontaneous behaviors.
(G) High correlation between the predicted responses and empirical neuronal activity in MOp, ACA and ENT during quiet wakefulness, grooming and novel object exploration, except for locomotion. C.C., Pearson's correlation coefficients.